Experiments in Fluids (2005) 38: 615–636
DOI 10.1007/s00348-005-0938-z

ORIGINALS

Ghanem F. Oweis · Steven L. Ceccio

Instantaneous and time-averaged flow fields of multiple vortices in the tip region of a ducted propulsor

Received: 9 October 2003 / Revised: 5 January 2005 / Accepted: 18 January 2005 / Published online: 24 March 2005

Abstract The instantaneous and time-averaged flow fields in the tip region of a ducted marine propulsor are examined. In this flow, a primary tip-leakage vortex interacts with a secondary, co-rotating trailing edge vortex and other co- and counter-rotating vorticity found in the blade wake. Planar particle imaging velocimetry (PIV) is used to examine the flow in a plane approximately perpendicular to the mean axis of the primary vortex. An identification procedure is used to characterize multiple regions of compact vorticity in the flow fields as series of Gaussian vortices. Significant differences are found between the vortex properties from the time-averaged flow fields and the average vortex properties identified in the instantaneous flow fields. Variability in the vortical flow field results from spatial wandering of the vortices, correlated fluctuations of the vortex strength and core size, and both correlated and uncorrelated fluctuations in the relative positions of the vortices. This variability leads to pseudo-turbulent velocity fluctuations. Corrections for some of this variability are performed on the instantaneous flow fields. The resulting processed flow fields reveal a significant increase in flow variability in a region relatively far downstream of the blade trailing edge, a phenomenon that is masked through the process of simple averaging. This increased flow variability is also accompanied by the inception of discrete vortex cavitation bubbles, which is an unexpected result, since the mean flow pressures in the region of inception are much higher than the vapor pressure of the liquid. This suggests that unresolved fine-scale vortex interactions and stretching may be occurring in the region of increased flow variability.

G. F. Oweis (✉) · S. L. Ceccio
Department of Mechanical Engineering,
University of Michigan, Ann Arbor,
MI 48109-2121, USA
E-mail: goweis@umich.edu

1 Introduction

The flow in the vicinity of the tip clearance and in the wake of ducted propellers and axial turbomachinery can be very complex. Lakshminarayana (1996) details many of the important flow processes, including the state of the boundary layer on the rotating blades and on the interior surface of the shroud, the production of flow jetting within the gap, the possible formation of "scraping vortices," and the interaction with regions of flow separation. The relative size of the tip clearance is an important parameter, along with the geometrical details of the blade tip and the blade loading distribution. A strong vortex can be created by the tip-leakage flow, and this vortex will interact with other concentrated vorticity shed by the blade, such as leading- and trailing-edge vortices. Both numerical and experimental studies of specific and canonical tip-leakage flows have been performed in order to understand and characterize the dominant flow features. See, for example, the surveys by Green (1995) and Spalart (1998), and the review in the von Karman Institute Lecture Series (1997).

Experimental examination of tip vortex flows is often complicated by the unsteadiness of the flow field. It is possible to correct pointwise measurements (such as Pitot tubes, hot-wire anemometers, and laser Doppler velocimetry (LDV) systems) of the vortical flow field for the effects of vortex "wandering" of single-line vortices if the wandering amplitude is small and the vortex is generally axisymmetric and without strong streamwise gradients (Baker et al. 1974). Measurement of more complex vortical flows (such as those having multiple vortices) with single-point measurements becomes problematic as the variability and complexity of the flow field increase. Consequently, interpretation of phase-averaged measurements in wakes of turbomachinery must be performed carefully in order to distinguish between "turbulent" fluctuations (i.e., those resulting from unresolved small-scale vorticity in the flow field)

and "pseudo-turbulent" fluctuations produced as a result of the cyclic variability of large-scale flow features.

Whole-field velocity measurements, such as particle imaging velocimetry (PIV), permit the examination of such variability, and such measurement techniques are now being implemented to examine complex flows in turbomachinery. Recent examples include the works of Day et al. (1996), Gogineni et al. (1997), Balzani et al. (2000), Wernet (2000), Judge et al. (2001), Uzol et al. (2002), Gopalan et al. (2002), and Chow et al. (2002). PIV permits the visualization of a plane or volume of fluid flow at a prescribed instance in time (a single realization). The timing of many of these realizations can then be phase-locked with the propeller angular position to produce phase-averaged mean and statistical information about the flow field.

In the present work, we will use planar PIV to visualize the vortical flow in the tip region of a ducted propulsor as it develops from the trailing edge of the blade. The process of vortex roll-up is examined as the "primary" tip-leakage vortex interacts with a trailing edge vortex and other, weaker vortices in the blade wake spiral. This flow has significant variability, and its analysis will be used to demonstrate how such variability can lead to significant differences between the "typical instantaneous" flow field and the simply averaged flow field. At a given propeller angular position, ~600 instantaneous PIV vector fields are acquired. Each instantaneous vector field is analyzed individually to obtain the location, strength, and other properties of the primary vortex, and the properties of other, secondary vortices. These properties can then be averaged from multiple vector fields to produce the mean properties of the "typical instantaneous" vortex. Additionally, the instantaneous vector fields can also be averaged first to give the simple average flow field (also referred to as the mean flow field or the time-averaged flow field), from which the mean-field vortex properties can be extracted. We will show that the analysis of the instantaneous flow fields can reveal important flow features that are lost in the time-averaged flow, such as the presence of multiple small-scale vortices, and the wide variation of the strength of the primary tip vortex. We will also show that there are significant differences between the vorticity distribution in the mean flow field and in the typical instantaneous flow field, and how the presence of multiple vortices in the instantaneous flow fields will affect the primary vortex properties in the phase-averaged flow field. We will also show how the variability and the presence of multiple uncorrelated vortices can lead to significant "pseudo-turbulence" after direct computation of the turbulence statistics.

Moreover, we will examine how these series of vortices roll up after the measured flow quantities have been partially corrected for flow variability. In the particular flow examined here, a region of increased vortex variability is discerned downstream of the blade through the corrected velocity fluctuations and also through the formation of incipient vortex cavitation. We show how the correctly scaled instantaneous flow fields reveal significant changes in the region near the location of cavitation inception. This suggests the presence of complex vortex–vortex interactions that may not be easily discernable with pointwise measurements or simply averaged planar flow realizations. However, this process can be revealed after careful post-processing to partially correct for flow variability.

2 Experimental setup

The experiments were performed in the David Taylor Model Basin (DTMB) 36-inch variable pressure recirculating water tunnel. A description of the water tunnel and test setup is provided by Chesnakas and Jessup (2003). The 36-inch diameter, open-jet test section was used for these investigations, and the propeller was driven using an upstream dynamometer. Inflow to the three-bladed propeller was uniform, except for the wakes from three upstream shaft support struts. The propeller shroud was a cylindrical extension of the water tunnel flow nozzle. This configuration produced an inner duct diameter of 0.864 m. The rotor had a diameter $D = 2 \times R_P = 0.85$ m, maintaining a tip clearance of $t_C = 6.7$ mm. The blade chord length, C, was a constant 0.381 m across the span. The blade thickness, t_B, approached 10% of the chord at the tip. The tip geometry was simple, with a constant 3.175-mm radius wrapped about the tip. The ratio of the tip clearance to the maximum thickness at the tip was 0.17, which is near the optimum value of 0.2 reported by Farrell and Billet (1994) to reduce the potential for tip-leakage cavitation. The propeller was made using a numerically controlled milling process and was manufactured to tolerances of approximately 0.1 mm from a mono-bloc 6061T6 aluminum forging. The blade section was a NACA 66, DTMB-modified thickness form, with a 0.8 mean-line camber. The trailing edges were thickened to incorporate a typical anti-singing bevel. The blade pitch was reduced at the hub and tip to minimize root and tip cavitation.

A planar PIV system was implemented for use in the water tunnel. Figure 1 shows a schematic drawing of the PIV setup. Two Quanta-Ray PRO-250 Series pulsed Nd:YAG lasers, placed outside the tunnel, with pulse energy of up to 800 mJ/pulse at 532 nm (green), were used to illuminate the flow. The two laser beams were combined and formed into a light sheet 5-mm thick and double-pulsed with a time separation varying between 6 μs and 20 μs for differing propeller speeds and varying distances from the blade trailing edge. A window was inserted into the duct to allow for optical access for the PIV laser sheet to the rotor flow, as shown in Figure 1b, c. The installation of the window produced a pocket in the duct. While no flow passed through the window, the presence of the pocket was not entirely passive. LDV measurements performed by Chesnakas

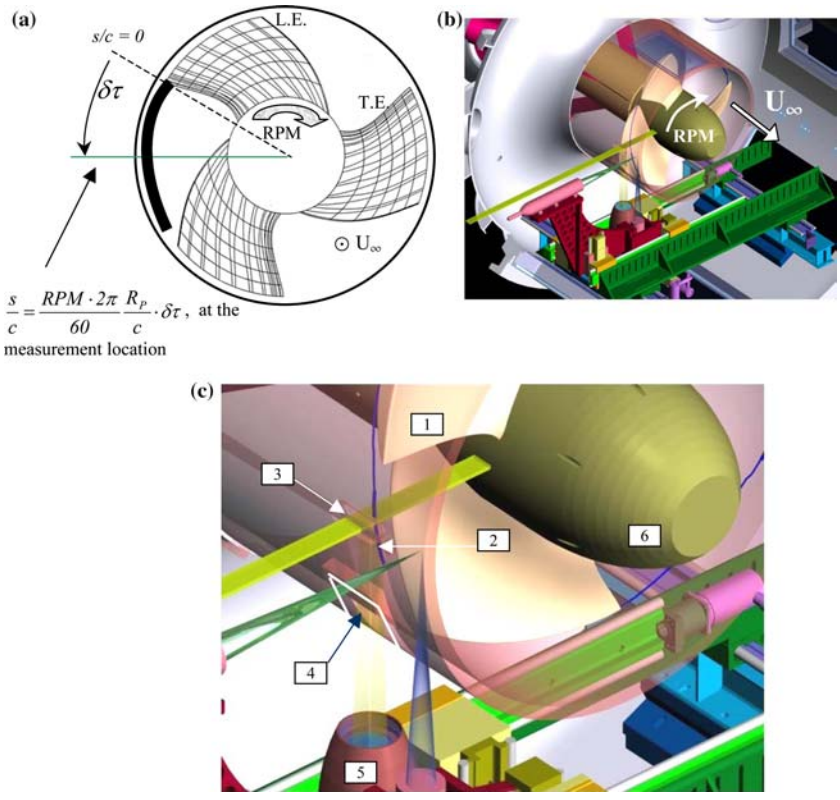

Fig. 1 **a** Front-view schematic (looking upstream) showing the propeller, the duct, and the tip vortex emanating near the trailing edge of a blade. Also shown is the coordinate system used. $\delta\tau$ is the time separation from the PIV measurement location along the vortex core to the blade trailing edge. The tunnel mean flow is out of the page. **b** Diagram of the open-jet test section of the David Taylor Model Basin 36-inch variable pressure cavitation tunnel with the three-bladed, ducted rotor P5206 installed. **c** Close-up view of the blade tip at the trailing edge (1), the emanating tip-leakage vortex on the inside of the duct—the dark curved line (2), the laser light sheet passing through a window installed in a pocket in the duct (3), another window in the duct to provide optical access for the camera (4), the underwater camera housing (5), and the hub (6) (Chesnakas and Jessup 2003)

and Jessup (2003) showed that the primary vortex moved slightly in and out of the pocket as the rotor blade passed by. However, this effect did not significantly alter the character of the flow in the tip region. The light sheet passed through windows in the outer wall of the test section and through the duct pocket to illuminate the flow. The sheet was oriented parallel to the propeller shaft axis, as shown in Fig. 1b. The digital camera used to record the flow images was mounted in a waterproof housing within the still-water region of the test section. The camera housing was mounted on a remotely controlled traverse, and the axial position of the camera was moved to place the mean center of the vortex near to the center of the image. An additional optical window was introduced in the shroud to provide optical access for the camera. The whole tunnel was seeded before the start of the experiments with silicon carbide particles of 1-μm mean diameter. A LaVision FlowMaster-3S PIV/PTV (particle image velocimetry/particle tracking velocimetry) system was used to control the firing of the lasers and to synchronize the image capture, which was achieved with a 1280×1024-pixel cross-correlation CCD camera. The camera had 12-bit resolution and ran at a 4-Hz repetition rate. The camera axis was perpendicular to the laser sheet and recorded the in-plane motion of the tracer particles. The light sheet was sufficiently thick to reduce the relative erroneous effect on the PIV measurements due to particles that entered or exited the light sheet during the laser double-pulse as a result of possible strong cross-plane flow velocities. The image field of view was 37.7×29.6 mm, and the lens on the camera was chosen to have a depth of field much larger than the thickness of the light sheet. The field of view spatial calibration was done by taking images of a registration target in the laser sheet plane. Images of the target were taken in the filled test section. The particles' images showed that the seeding distribution was uniform over the field of view, and no dispersion of particles away from the vortex center was noticed. A multi-pass algorithm (DaVis6.0.4) was used to compute the in-plane velocity vectors using 32×32-pixel interrogation windows with 15% overlap applied in the final pass. This produced a velocity field with 46×37 vectors at a 0.83-mm vector spacing. A median filter was used to remove outliers from the velocity vector field by comparing each vector to the root mean square value of its neighbors, and the rejected vectors were substituted by interpolation between the surrounding cells. Timing of the PIV image capture was synchronized with the passage of the rotor blades, making it possible to capture multiple images at a given blade position for phase averaging. The images were taken at various downstream distances along the pitch line, s, with $s = 0$ being at the trailing edge and tip of the selected blade. The pitch line is the azimuthal line (circular arc) drawn by the blade tip at the trailing edge. The distance s is calculated by knowledge of the propeller tip velocity and the time elapsed from the position of the trailing edge at the tip to the laser light sheet. All flow fields presented in this work are tagged with known blade positions (propeller angular positions). The velocity vectors were used to compute the vorticity field

by making use of Stokes' theorem. The vorticity at a point was calculated from the line integral of the velocity vector around a closed loop enclosing the point under consideration divided by the total area enclosed by the loop. On the experimental grid, the integration path was composed of connected line segments chosen to pass through the centers of the eight immediate cells neighboring the cell of interest. For the cells on the edges of the PIV field of view, the vorticity was calculated using forward and backward differentiation schemes. After the vorticity field was calculated, a 3×3 mean filter was used to reduce the noise.

A discussion of the propagation of measurement errors to derived quantities is given by Figliola and Beasley (2000). Discussion of errors in vorticity from PIV measurements is discussed by Fouras and Soria (1998) and Raffel et al. 1998). Fouras and Soria (1998) divide the uncertainty into bias and random errors, with the bias errors being dependent mainly on the differentiation scheme applied, while the random errors propagate from the uncertainty in the velocity measurement.

Some of the factors contributing to the error in the PIV velocity measurements include image magnification factor, particle image size, seeding density, cross-plane velocity, interrogation area overlap, laser pulse timing, and laser energy. Care was taken in conducting the experiments to optimize each of these factors. The interrogation area overlap in the vector extraction algorithm was set to 15% to account for particles that have crossed the interrogation window, without data over-sampling which produces correlated velocity measurements in neighboring cells. Raffel et. al. (1998) discuss the increased noise levels in vorticity calculation from over-sampled PIV velocity data. The velocity uncertainty in the reported PIV measurements is estimated at 5%.

The bias error in vorticity calculations as discussed by Fouras and Soria (1998) is expected to be small. Figures 4 and 15 in Fouras and Soria (1998) show that, when there are approximately 12 vectors spanning the core of a Gaussian vortex, the maximum bias error in vorticity, which corresponds to the vorticity peak at the vortex center, is around 5%. In this study, the typical number of vectors on a line spanning the core of the primary vortex varied between 8 and 16, indicating that the bias error in the peak vorticity incurred due to spatial resolution is near 5%. Moreover, the method used in calculating the vorticity in this study has been shown by Raffel et al. (1998) to be superior to other methods, such as center differencing and Richardson interpolation with regard to the incurred uncertainty in vorticity, since 12 independent data points are used in the calculation. A cumulative uncertainty in vorticity is estimated to be 15%.

The rotor was operated at a constant advance coefficient $J = U_T/nD$, where U_T is the average flow speed into the duct (m/s), n is the rotational speed of the rotor (rps), and D is the rotor diameter (m). The operating advance coefficient was selected to produce a typical leakage vortex, without unwanted flow conditions over the blade, with $J = 0.971$. This is higher than the design advance coefficient $J = 0.75$ in order to avoid the formation of the leakage vortex at the leading edge of the blade and the occurrence of pressure-side leading edge cavitation near the blade tip. Several rotational speeds, n, and mean axial velocities, U_∞, were examined. Presented in this work are typical results for the mid-range Reynolds number ($Re = 7\times10^6$) corresponding to a rotational speed of 375 RPM and a free-stream velocity $U_\infty = 5.24$ m/s. The Reynolds number is based on the chord length, c, and the total tip velocity, $(U_\infty + \pi Dn)$. The inlet absolute static pressure was maintained high enough ($P_\infty = 309$ kPa at 500 RPM) during the PIV measurements to suppress cavitation. This advance coefficient resulted in a thrust coefficient $K_T = T/\rho n^2 D^4 = 0.31$ and a torque coefficient $K_Q = Q/\rho n^2 D^5 = 0.054$ that did not vary over the range of Reynolds numbers studied, 4.6×10^6 to 9.2×10^6, corresponding to propeller rotation speeds of 250 RPM to 500 RPM, respectively. See Oweis et al.(2005a, b) for additional details. Application of roughness to the leading edge of the rotor blades did not significantly influence the measured results. Moreover, the blade-to-blade variations in the measured vortex quantities were insignificant, since they were of the same order as the realization-to-realization variability on one given blade.

3 Overall development of the tip-leakage flow

Both the LDV measurements performed by Chesnakas and Jessup (2003) and the PIV measurements discussed in this paper reveal the general development of the flow in the tip region of the rotor. The pressure difference across the blade produces a flow through the tip region and causes the formation of a strong tip-leakage vortex, which we will refer to as the primary vortex. A second co-rotating concentrated vortex forms at the trailing edge, and we will refer to this as the secondary vortex. Additionally, there were multiple, secondary, co-rotating vortices of comparable or weaker strength. Counter-rotating secondary vortices were also present. Figure 2 shows the primary and secondary vortices visualized by cavitation in their respective cores. In addition, concentrated vorticity is also present in the blade wake. The mean axes of the primary and secondary vortices are not necessarily perpendicular to the plane made by the PIV light sheet, but the most part of the vorticity is in this plane, as will be discussed below.

The time-averaged flow fields show that the secondary vortices merge with the primary vortex into a single structure within a distance of nearly $0.25C$ downstream from the blade trailing edge. The basic process of vortex merger has been examined by many researchers. Co-rotating vortices can orbit and merge together, forming a single vortex as they "roll up" (see, for example, Green 1995 and Spalart 1998). Devenport et al.

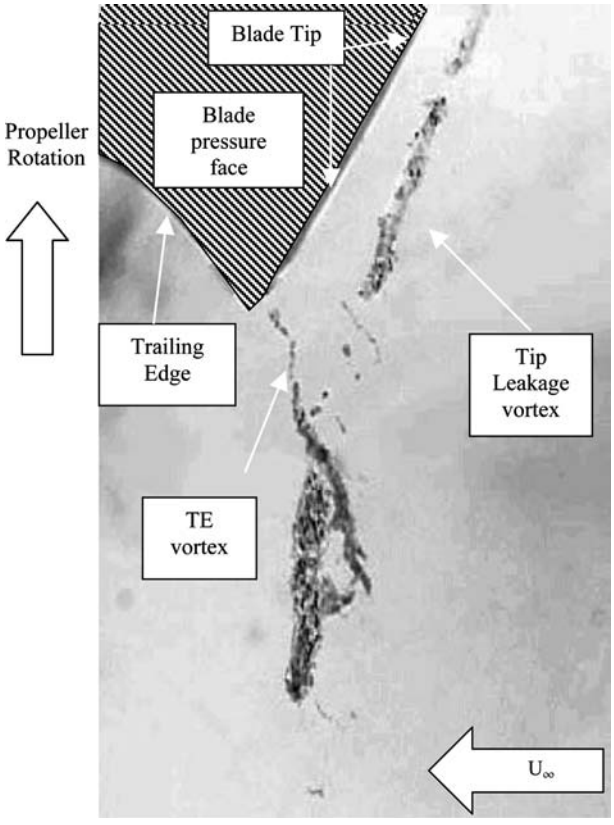

Fig. 2 Side-view photograph of the blade trailing edge taken through a clear section of the duct. The pressure has been lowered and developed vortex cavitation visualizes the tip-leakage and trailing edge (TE) vortices. The cavitation number is $\sigma = 5.6$ (Chesnakas and Jessup 2003)

(1999) examined the structure of the combining equal-strength pair in detail, with particular emphasis on the turbulent flow formed during the vortex merger. They showed that the orbiting vortices ultimately combine in a strongly unsteady flow that may be accompanied by the formation of smaller vortex filaments that are not parallel to the primary axes of the merging vortices, but are oriented in the cross-stream direction and are, consequently, stretched during the final stages of the merging. Additionally, a series of smaller vortices associated with the blade wake are rolled into the primary and secondary vortices.

The merger of co-rotating Gaussian vortices of unequal strength has been examined experimentally by Chen et al. (1999). These researchers found that the weaker vortex can wrap around the stronger vortex—in a three-dimensional flow characterized by vortex stretching—and fragment into filaments prior to merger. The direction in which the weaker vortex splits, whether radial or axial, depends on the relative vortices' circulations before the merger. The circulation was conserved before and after the merger. Devenport et al. (1997) and Ortega et al. (2003) examined the interaction of unequal strength counter-rotating vortex pairs, the latter observing complex wrapping and stretching of the weaker vortex. Such interactions often occur relatively far downstream of the vortices' origin. In the present investigation, we have multiple co-rotating vortices of varying strengths that are rolling up in the wake of the blade. Weak, counter-rotating secondary vortices are also present in the flow field. We will show that the complex mechanisms revealed by the studies cited in this section are likely at work in this flow as well.

4 Analysis of individual PIV images

As discussed above, the flow in the propeller wake region is composed of multiple co- and counter-rotating vortices of varying strengths. It is possible to reduce the in-plane vorticity distribution into a sum of discrete, two-dimensional axisymmetric Gaussian vortices, which can then be used to reconstruct the original flow field. Also known as the (time-invariant) Lamb-Oseen vortex (Green 1995), the distributions of the circumferential velocity $u_\theta(r)$, vorticity $\omega(r)$, and circulation $\Gamma(r)$, as a function of the radial distance, r, are given by:

$$u_\theta(r) = \frac{\Gamma_O}{2\pi r}\left(1 - e^{-\eta_1 (r/a)^2}\right) \tag{1}$$

$$\omega(r) = \frac{\Gamma_O}{\pi}\frac{\eta_1}{a^2} e^{-\eta_1 (r/a)^2} \tag{2}$$

$$\Gamma(r) = \Gamma_O\left(1 - e^{-\eta_1 (r/a)^2}\right) \tag{3}$$

where $\eta_1 = (1.121)^2 = 1.257$, and the core radius, a, is defined as the radius where maximum tangential velocity, u_C, occurs. The latter is given by:

$$u_C = \eta_2 \frac{\Gamma_O}{2\pi a} \tag{4}$$

with $\eta_2 = 0.715$. Integration of the radial momentum equation yields the pressure dip at the vortex centerline, $r = 0$:

$$\Delta P = p_C - p_\infty = -\eta_3 \rho_f \left(\frac{\Gamma_O}{2\pi a}\right)^2 \tag{5}$$

where $\eta_3 = 0.870$ (Oweis et al. 2004) and p_∞ is the pressure far from the vortex.

In reality, the flow also has vorticity components parallel to the PIV plane as well as flow non-uniformity in the cross-plane direction. However, most of the vorticity is captured in the PIV measurement plane. The series of Gaussian vortices used to fit and reconstruct the actual in-plane flow can be used to scale the resulting vortex-induced pressure variations. Two parameters are needed to characterize each vortex: the core radius, a_i, and the total circulation $\Gamma_{O,i}$. Hereafter, the subscript i identifies the vortex in question, where $i = 1$ is the strongest (largest circulation) or "primary" vortex, and the remaining identified vortices ($i > 1$) are "secondary."

An identification procedure was used to find and fit Gaussian vortices to the regions of concentrated

vorticity in each PIV field. First, the velocity field was used to create a field of cross-plane vorticity magnitude. Next, a vorticity threshold (1.4 times the average of the absolute magnitude of the vorticity of the whole field) was applied to locate the local peaks of vorticity. The core size and strength of each of the identified vortices were then measured, compared, and fitted to the best Gaussian vortex. Ideally, the core radius (a) would be identified by the distance from the vortex center to the location where the tangential velocity reaches a maximum. This is not possible when there are multiple vortices in close proximity. Consider, as an example, the case where the centers of two identical co-rotating planar vortices are separated by one core diameter ($2a$). At the midpoint of the line connecting the two centers, the tangential velocity is zero because the velocity contributions from each of the vortices cancel. In such cases, it becomes difficult to identify where the core limit of one vortex begins and where the core of a neighboring vortex ends (see also Copland et al. 1998). Alternatively, the core can be identified using the gradient of circulation. Differentiating Eq. 3 with respect to r reveals that the gradient of circulation, $\mathrm{d}\Gamma/\mathrm{d}r$, reaches a maximum at $r = a/(2\eta_1)^{1/2} = 0.631a$. The location of this maximum is also influenced by the vorticity fields of the neighboring vortices, but this effect is small since the vorticity contributions of the nearby vortices decrease very quickly with distance from their respective centers. Thus, the identification of each vortex was performed by first examining the gradient of circulation for each concentration of vorticity. The core radius (a) could then be extrapolated through dividing the radius of maximum $\mathrm{d}\Gamma(r)/\mathrm{d}r$ by 0.631.

For each concentration of vorticity, the circulation $\Gamma_k(r)$ and its derivative $\mathrm{d}\Gamma_k(r)/\mathrm{d}r$ were calculated along 26 evenly distributed radial lines around the center ($k = 1, 2, 3, \ldots, 26$). The radius at which the peak in $\mathrm{d}\Gamma_k(r)/\mathrm{d}r$ occurred was noted, and this was extrapolated to find the core radius a_k for radial line k. The radial position of the vortex core border from each of the 26 evenly distributed lines was marked by a point, and, by connecting the points serially, the core contour was defined. The core radius was defined as the radius of a circle with an area equal to that enclosed by the core contour. A five-point moving average filter was used to correct outlying measurements in the 26 points. A no-overlap condition between the different vortex cores was imposed. The core circulation $\Gamma_i(a_i)$ for a given vortex i was calculated from the area integral of the vorticity inside the core contour ($0 < r < a_i$). The total vortex circulation ($0 < r < \infty$) was computed from $\Gamma_{\mathrm{O},i} = \Gamma_i(a_i)/(1 - \mathrm{e}^{-\eta_1}) = 1.398\,\Gamma_i(a_i)$. The vortex centroid location, $\mathbf{x}$, was calculated from $x = \int_{\text{Core area}} x\omega.\mathrm{d}A \Big/ \int_{\text{Core area}} \omega.\mathrm{d}A$ Typically, the deviation of the centroid location from the point of peak vorticity, which resulted from the asymmetry of the vortex structure, was small.

The average number of vortices in a typical PIV field was between 5 and 6, while the number varied between 1 and 15 among different flow realizations. For each image, the correlation between the original and the identified velocity and vorticity fields was examined. The identified vortices from the identification procedure were used to reconstruct the velocity and vorticity fields. The reconstructed velocity field was computed by superposing, on a grid similar to the PIV experimental grid, the velocity contributions of Gaussian vortices with core radii, strengths, and center loci identical to those of the identified vortices. A mean velocity component that maximized the goodness-of-fit was added to the velocity field. The value of this component was typically small compared to the peak vortex velocity. The vorticity field was reconstructed by algebraic summation of the contributions of each of the Gaussian vortices on the grid. In some cases, the identified vortex was significantly distorted and stretched in a certain direction, and so, a distribution of three overlapping identical Gaussian vortices (forming nearly an elliptical vortex) with the same equivalent circulation and almost the same area as the original vortex was used for the reconstruction, rather than fitting a single vortex. Correlation values for the velocity field, R_{V}^2, and for the vorticity field, $R_{\omega}{}^2$, were computed for each instantaneous flow field:

$$R_{\mathrm{V}}^2 = 1 - \frac{\sum_{i=1}^{j} (V_{\mathrm{M},i} - V_{\mathrm{C},i})^2}{\sum_{i=1}^{j} (V_{\mathrm{M},i} - \bar{V}_{\mathrm{M}})^2}, \qquad R_{\omega}^2 = 1 - \frac{\sum_{i=1}^{j} (\omega_{\mathrm{M},i} - \omega_{\mathrm{C},i})^2}{\sum_{i=1}^{j} (\omega_{\mathrm{M},i} - \bar{\omega}_{\mathrm{M}})^2} \tag{6}$$

where the subscripts M and C denote the measured (PIV) and the computed (reconstructed) fields, respectively, for the total number of cells j. The correlation values give a measure of the goodness-of-fit between the reconstructed and the experimental PIV field. An R^2 value of 1 signifies a perfect fit, while a value of 0 indicates that the fitted function is only as good as fitting the data with a constant value equivalent to the mean of the experimental data.

Once each vortex concentration was identified, an iterative optimization scheme was used to find the best core radius and circulation of each of the vortices to maximize the vorticity field correlation. This was done simultaneously for all the vortices by trying slightly different values above and below the initially identified quantities. For instance, the core size optimization was implemented within approximately $\pm$half a PIV vector spacing. Figure 3 shows a typical PIV field and the reconstructed field. In this case, 12 concentrations of vorticity are identified, and the reconstruction yields $R_{\mathrm{V}}^2 = 0.88$ and $R_{\omega}{}^2 = 0.86$. This figure shows the presence of a primary vortex surrounded by a number of co-rotating secondary vortices. Moreover, these secondary vortices are also surrounded by a number of concentrated regions of opposite-signed vorticity. The number of identified counter-rotating vortices (with negative vorticity) is substantially less than the co-rotating vortices, even though, visually, their actual

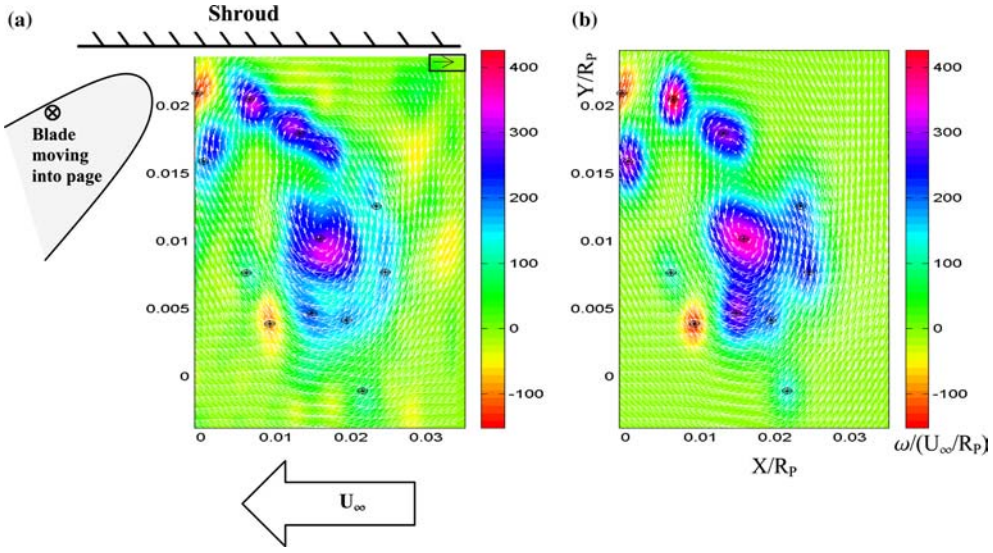

Fig. 3 **a** An instantaneous PIV velocity vector field with vorticity contours taken at $s/c = 0.03$ and 500 rpm. The *crosses* indicate the centroids of identified vortices, and the reference arrow (*top right corner*) is 15 m/s. **b** The reconstructed velocity vector field with vorticity contours computed from superposing Gaussian vortices using the vortex locations, strengths, and sizes identified from the field in **a**. The R^2 values based on the vorticity and velocity fields are 88% and 86%, respectively. Notice that a number of vortices with negative vorticity are not identified because their absolute peak vorticity values were below the cutoff level

numbers are comparably close. This is because the counter-rotating vortices have vorticity peak magnitudes that are below the cutoff level and, thus, they are not detected in the vortex identification scheme. Figure 4 shows a histogram of R_V^2 and R_ω^2 for all of the PIV images examined, as a function of downstream location, s/c. From the vorticity correlations, the best fits occur at the trailing edge $s/c = 0.03$, and, with further distance downstream of the trailing edge, the mean value of the correlation distribution drops. At $s/c = 0.46$, the lower end tail of the vorticity correlation coefficient histogram, R_ω^2 grows, suggesting that the vortices get less Gaussian at this spatial position. The correlation coefficients based on the velocity field R_V^2 display a similar trend, except for $s/c = 0.46$, where the correlations tend to improve. This is because the number of secondary vortices increases and their spatial positions become more evenly distributed around the primary vortex with increasing downstream distance. Thus, the velocity field, which is an integral effect of all the vortices, becomes less asymmetric, and the summed circulation of the identified vortices becomes the dominant parameter when reconstructing the velocity field. This decomposition of vorticity is used below to examine the evolution of the merging vortices and the variability of the flow field.

5 The averaged flow field

PIV images were collected for multiple downstream positions, s/c, along the vortex path. The images were collected for an individual blade to eliminate flow variability due to small blade-to-blade variations. 586 images were collected at each of the downstream locations. Figure 5a shows the average vorticity contours for $s/c = -0.02$, 0.03, 0.11, 0.23, 0.34, and 0.46. For $s/c = -0.02$, the trailing edge of the blade is about to intersect the PIV plane, while for $s/c = 0.03$, the trailing

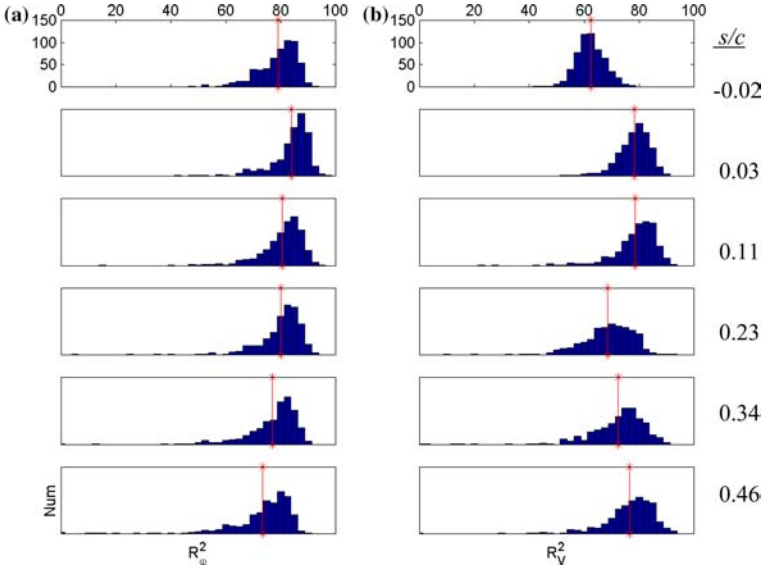

Fig. 4a, b Histograms of the correlation coefficients of the reconstructed fields. **a** The vorticity correlations R_ω^2 and **b** the velocity correlations R_V^2 for six spatial positions downstream of the blade trailing edge, s/c. The *vertical lines* indicate the mean value of each distribution

edge has just left the PIV plane. The identification process described in Sect. 4 is used to find the cores of the vortices in the averaged flow fields, and these are also delineated in the figure. Near the trailing edge, 2 or 3 strong vortices are identified, but by $s/c = 0.46$, the average flow field has been reduced to a single vortex structure. Figure 5b shows the average flow field reconstructed from the individual vortices identified in the instantaneous flow fields. The experimental time-averaged fields and the reconstructed time-averaged fields are very similar, indicating that the identification process captures the largest portion of the vorticity that contributes to the average flow properties.

The roll-up characteristics of the identified concentrated vortices are illustrated in Fig. 6. Presented in Fig. 6a are the circulation values of the vortices identified from the average flow fields, plotted as a function of downstream distance, s/c. The total average circulation, $\sum_i \overline{\Gamma_{O,i}/U_\infty R_P}$, stays nearly the same as the three strongest average vortices merge. The circulation of the strongest identified vortex (primary vortex, or vortex having the largest circulation), $\overline{\Gamma_{O,1}}$, increases just slightly as the smaller vortices are lost. Henceforth, an over-bar will signify quantities identified in the *mean flow field*, whilst angled brackets will represent mean quantities identified in the *instantaneous flow fields*. For example, $\overline{\Gamma_{O,1}}$ is the strength of the primary vortex identified in the mean field created after averaging all the

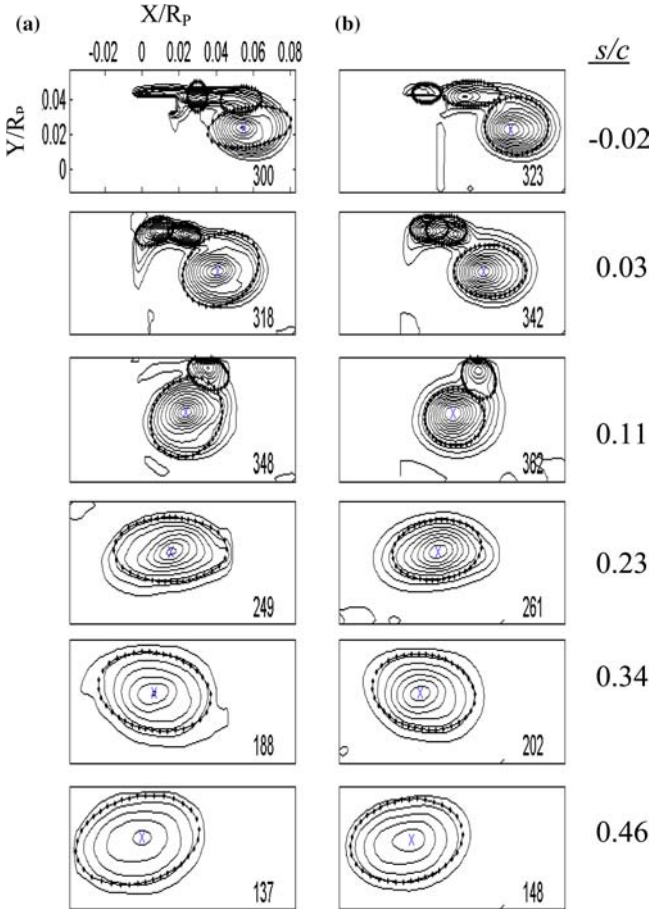

Fig. 5 **a** Vorticity contours $\overline{\omega/(U_\infty/R_P)}$ measured downstream of a single blade for varying s/c. At $s/c = 0.0$, the trailing edge near the blade tip is in the visualized plane. The *ellipses*/*circles* indicate the cores of the identified vortices in the image. **b** The reconstructed vorticity field from the identified vortices. The *crosses* identify the center of the primary vortex, and the numerical value is the value of the vorticity at that location. The difference in vorticity contour level between any two consecutive contour lines is the same for all plots

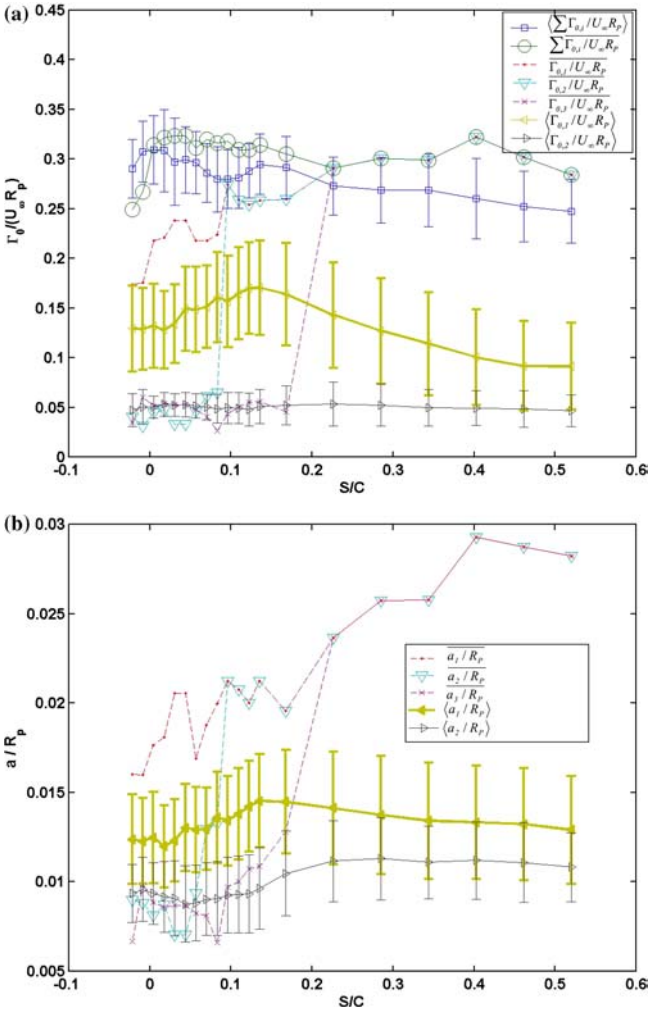

Fig. 6 **a** Evolution of the identified circulation with downstream distance s/c; (*red dots*) $\overline{\Gamma_{O,1}/U_\infty R_P}$, (*blue inverted triangles*) $\overline{\Gamma_{O,2}/U_\infty R_P}$, (*crosses*) $\overline{\Gamma_{O,3}/U_\infty R_P}$, and (*green circles*) is the total identified circulation in the average flow field, $\sum_i \overline{\Gamma_{O,i}/U_\infty R_P}$. Also shown are the averages of the instantaneous identified circulations for the primary and secondary vortices, (*yellow triangles*) $\langle \Gamma_{O,1}/U_\infty R_P \rangle$, (*black triangles*) $\langle \Gamma_{O,2}/U_\infty R_P \rangle$, respectively, and (*purple squares*) is the total, instantaneous identified circulation of all vortices $\langle \sum_i \Gamma_{O,i}/U_\infty R_P \rangle$. **b** Evolution of the identified core radii with downstream distance; (*red dots*) $\overline{a_1/R_P}$, (*blue inverted triangles*) $\overline{a_2/R_P}$, (*crosses*) $\overline{a_3/R_P}$, (*yellow triangles*) $\langle a_1/R_P \rangle$, and (*black triangles*) $\langle a_2/R_P \rangle$. The *bars* represent $\pm$one standard deviation (a measure of the cyclic variability in the flow properties)

vector fields, while $\langle \Gamma_{O,1} \rangle$ is the average strength of the primary vortex identified from the instantaneous flow fields. In the angle bracket quantities, the averaging is done on the given quantity after it has been identified in the instantaneous flow fields. Plotted in Fig. 6b are the core radii, $\overline{ai}/R_P$, for $i = 1$, 2, and 3. The primary vortex core size in the time-averaged field increases with downstream distance. It is interesting to note that there is more variation in the core size of the primary vortex identified in the time-averaged field ($\overline{a_1}/R_P$) with downstream distance compared to the average core size of the primary vortex identified in the instantaneous flow fields ($\langle a_1 \rangle / R_P$). This is due to the cyclic variation of the instantaneous positions of the secondary vortices with respect to the axes of the primary vortex and the other secondary vortices, which creates smooth vorticity bridges between the multiple vortices in the time-averaged field. At early s/c positions, the vortices are spaced far enough apart and they do not wander significantly, so that they are still distinct in the averaged flow field, while, in further downstream positions, the vortices are essentially merged by the averaging process. This leads to the sharp variation in $\overline{a_1}/R_P$ with s/c.

As might be expected, the interpretation of these average flow fields must be performed with caution. Previous researchers have explored how the wandering of a single vortex can influence the time-averaged flow field (see, for example, Baker et al. 1974, Straka and Farrel 1992, Devenport et al. 1996, and Boulon et al. 1999). If a Gaussian vortex undergoes random isotropic wandering, the resulting average flow field will also be a Gaussian vortex with decreased maximum tangential velocity and increased core radius. If the standard deviation of the wandering amplitude is κ, the maximum tangential velocity and core radius of the averaged vortex are given by:

$$\bar{u}_C = \frac{u_C \cdot a}{\bar{a}} \tag{7}$$

$$\bar{a} = \sqrt{2\eta_1 \kappa^2 + a^2} \tag{8}$$

indicating that the strengths of the instantaneous and averaged vortices are equal, $\bar{\Gamma}_O = \Gamma_O$. A wandering amplitude of $\kappa/a = 0.25$ will yield $\bar{a}/a = 1.08$, $\kappa/a = 0.50$ yields $\bar{a}/a = 1.28$, and $\kappa/a = 1.0$ results in $\bar{a}/a = 1.87$. Consequently, vortex wandering with amplitudes greater than about half of the true (instantaneous) core size will result in significant differences between the instantaneous and the time-averaged flow fields.

In the tip-leakage vortex flow under consideration, multiple complications arise in addition to the wandering of the primary vortex. First, there are multiple concentrated vortices present. Second, between different realizations of the flow, the number of concentrated vortices varies. And third, the strengths and locations of the vortices vary between different realizations of the flow at a given propeller angular position. These complexities lead to significant differences between the averaged flow field and the typical instantaneous flow, as demonstrated in Figure 6. Plotted in Fig. 6a is the average of the instantaneous circulation of the strongest identified vortex (primary vortex), $\langle \Gamma_{O,1}/U_\infty R_P \rangle$, as a function of s/c. Remember, angled brackets represent quantities averaged after being identified in the instantaneous vortex flow fields. The total identified circulation is also plotted, $\left\langle \sum_i \Gamma_{O,i}/U_\infty R_P \right\rangle$. Note that the mean circulation of the instantaneous strongest identified vortex, $\langle \Gamma_{O,1}/U_\infty R_P \rangle$, is at least 50% less than that of the strongest vortex identified in the averaged flow field, $\overline{\Gamma_{O,1}/U_\infty R_P}$. The circulation of the strongest instantaneous vortex, $\langle \Gamma_{O,1}/U_\infty R_P \rangle$, slowly decreases with increasing s/c, while the circulation of the strongest vortex identified in the mean field, $\overline{\Gamma_{O,1}/U_\infty R_P}$, generally remains the same or increases. Notice the vertical bars in the figure indicate the extent of the measured cyclic variations in the vortex properties, and are not error (uncertainty) bars. The total instantaneous circulation identified in all the vortices is slightly less than the total identified circulation in the averaged flow. But, generally, the mean field total circulation is within the one standard deviation limit of the instantaneous total circulation, suggesting that the vortex identification procedure captures most of the flow vortices. The evolution of the instantaneous mean quantities with s/c is smoother than that of the properties identified in the average flow field. Also, the second strongest vortex is still identified in the instantaneous fields, even when it has been averaged out in the mean field. Similarly, in Fig. 6b, the instantaneous core size of the strongest vortex, $\langle a_1/R_P \rangle$, is substantially smaller than its counterpart identified in the mean flow field. The instantaneous core size, $\langle a_1/R_P \rangle$, does not increase with increasing s/c, while the core size of the mean flow field vortex, $\overline{a_1/R_P}$, increases substantially.

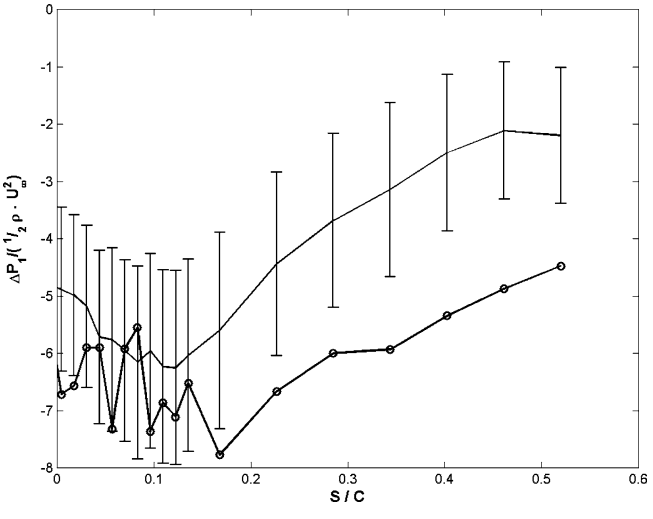

Fig. 7 The pressure coefficient of the primary vortex, $C_{P,1} = \Delta P_1 / \frac{1}{2}\rho U_\infty^2$, as a function of the downstream distance s/c; (*open circles*) $\overline{C_{P,1}}$, and (*solid line*) $\langle C_{P,1} \rangle$, along with range $\pm$ one standard deviation

Figure 7 shows the evolution of the pressure coefficient, $C_{P,1} = \Delta P_1 / \frac{1}{2}\rho U_\infty^2$, of the primary vortex with downstream location. The pressure is computed using Eq. 5. While the true pressure at the location of the vortex core is affected by the presence of the surrounding vortices and the three-dimensionality of the flow, the pressure computed here will scale the pressure deficit due to the local concentration of vorticity. The lowest pressure drop in the primary vortex core occurs for $0.1 < s/c < 0.2$ for both the mean flow primary vortex and the primary vortex from the instantaneous fields. The pressure inside the core begins to recover after this downstream location. Note that analysis of the mean flow vortex suggests a pressure coefficient that is substantially larger in absolute magnitude than that inferred from the instantaneous vortex properties. The fluctuations in the mean flow vortex pressure coefficient for $s/c < 0.2$ are primarily due to the difficulty encountered in discerning the exact perimeter of the vortex core.

6 Variability of the instantaneous flow fields

As shown by the large variations in the identified vortex circulation and core size, significant variability exists between different instantaneous realizations of the flow. Figure 8a presents histograms showing the number of vortices, N, identified in each image. N increases with s/c, and there is significant variation of the form of the distribution. Figures 8b–d present histograms of the quantities $\Gamma_{O,1}/U_\infty R_P$, a_1/R_P, and $C_{P,1}$, all for the strongest identified vortex (primary vortex). Also plotted are vertical lines delineating the mean values of the histograms. Significant variability is present. For example, it is possible to have an instantaneous vortex that has twice the circulation of the typical vortex. Also, the distributions of the variables do not follow any canonical form. Note the changes in the forms of the distributions of the circulation and pressure coefficient between $s/c = 0.23$ and 0.46. This will be discussed further below.

Plotted in Fig. 9a are the locations of the primary identified vortices. In Fig. 9b are the locations of the secondary co-rotating vortices, and in Fig. 9c are the locations of the secondary counter-rotating vortices. These data reveal the degree to which the vortices change position from one instantaneous realization of the flow to another. The extent of wandering of the primary vortex increases with increasing downstream distance, and this is also shown by the histograms of $\Delta r_1/R_P = \left[\left((x_1 - \overline{x_1})^2 + (y_1 - \overline{y_1})^2\right)^{1/2}\right] \Big/ R_P$, the displacement of the instantaneous primary vortex center from the position of the mean vortex center (Fig. 9d). The histograms become broader with increasing downstream distance, showing increased vortex wandering.

The relative positions of the secondary vortices with respect to the primary vortex are shown in Fig. 10a. The orbit of the secondary vortices around the primary vortex is discernable up to $s/c = 0.23$. Further downstream, the relative positions of the secondary vortices become more variable. This is quantified with the histograms of the inclination angle of the line segment between the secondary and primary vortex centers, $\theta_{i1} = \tan^{-1}[(y_1 - y_i)/(x_1 - x_i)]$, $i > 1$, in Fig. 10b, and the relative distance between the primary and secondary vortices, $\Delta r_{i1}/R_P = [(x_1 - x_i)^2 + (y_1 - y_i)^2]^{1/2}/R_P$, in Fig. 10c. $\theta_{1,i}$ occurs in narrow bands near the trailing edge, indicating a stronger correlation between the positions of the primary and secondary vortices, and it becomes more evenly distributed with downstream distance, showing a reduced correlation. It is interesting to note that, for $s/c > 0.11$, where the clustering of secondary vortices in an orbit around

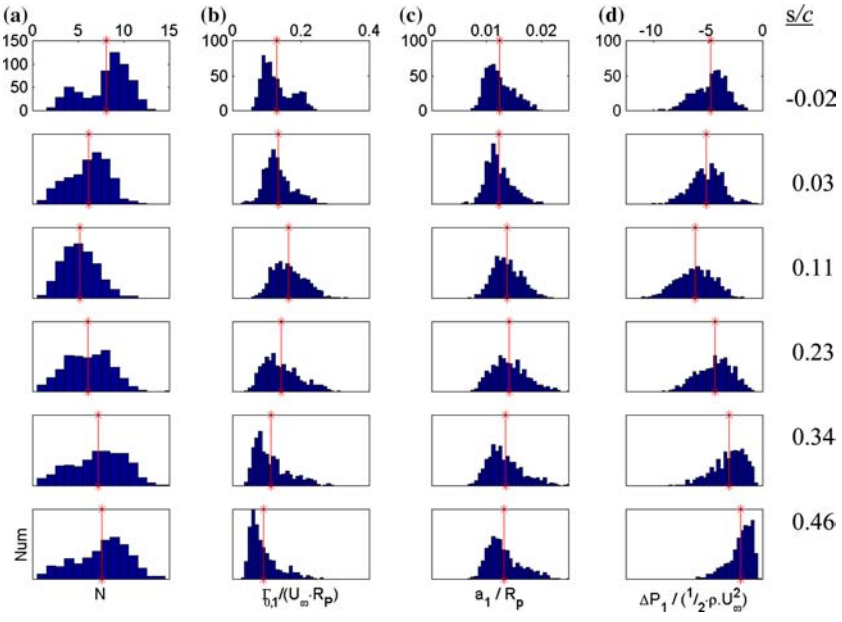

Fig. 8 **a** Histograms of the number of identified vortices in each instantaneous field, N. **b** The circulation of the instantaneous primary vortex, $\Gamma_{O,1}/U_\infty R_P$. **c** The core radius of the primary vortex, a_1/R_P. **d** The inferred pressure coefficient of the primary vortex $C_{P,1}$. The *vertical lines* indicate the mean value of each distribution

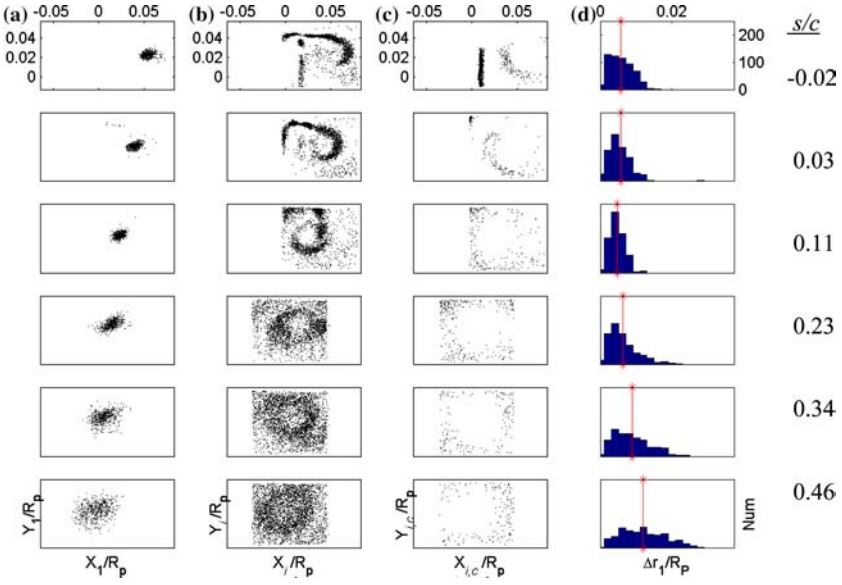

Fig. 9 **a** Scatter plots of the instantaneous locations of the primary vortex [x_1/R_P, y_1/R_P]. **b** Locations of the secondary co-rotating vortices [x_i/R_P, y_i/R_P] for $i>1$ **c** Locations of the counter-rotating vortices. **d** Histograms of the relative distance of the instantaneous primary vortex to the primary vortex identified in the mean flow field, $\Delta r_1/R_P = \left[\left((x_1-\overline{x_1})^2 + (y_1-\overline{y_1})^2\right)^{1/2}\right] \Big/ R_P$. The *vertical lines* indicate the mean values of the histograms

the primary vortex becomes less obvious, the Δr_{i1} histograms become similar.

The identified vortex strength is strongly correlated to the core radius, as shown in Fig. 11. Figure 11a is a plot of $\Gamma_{O,1}/U_\infty R_P$ and a_1/R_P for the strongest vortex (or primary vortex, $i=1$), and Fig. 11b shows the correlation for the strongest three *secondary* vortices ($i=2$, 3, 4). It can be noted that some of these secondary vortices are, in fact, counter-rotating. The statistical correlation coefficients for these data are approximately 90%. The figure shows significant vortex variability, one source of which could be variations in the angle that the vortex makes with the planar imaging volume, λ. If an axisymmetric Gaussian line vortex of core size a intersects a plane, the loci of the points that identify the position of maximum tangential velocity will form an ellipse, and the equivalent radius of the ellipse will be $a_\gamma = a(\sec\lambda)^{1/2}$. A tilt angle of 10° results in an overestimate of the radius by 1%, and a tilt of 30° results in a 7% overestimate. The circulation calculated around the elliptical contour will remain the same as that of the original, un-tilted circular contour, by the Helmholtz theorem. Consequently, the effect of moderate tilting (less than 30°, say) will not lead to very large changes in the measured core size and circulation, and the correlation between these quantities shown in Fig. 11 is not primarily due to this three-dimensional effect. Instead, the nearly constant slope suggests that the primary vortex maximum tangential velocity, U_C, remains relatively constant from one revolution to another; it is the core size that varies. This would be the result if the vortex maximum tangential velocity scales with the propeller tip speed, while the variable core size is governed by the vortex detachment from the tip as well as possible flow separation in the tip region.

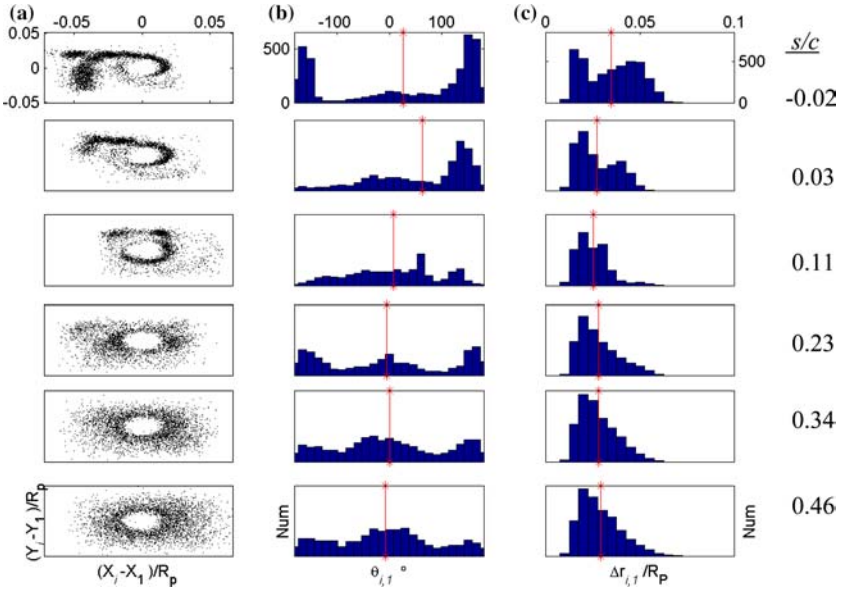

Fig. 10 **a** Scatter plots of the relative location of the secondary vortices from the location of the primary vortex, [$(x_i-x_1)/R_P$, $(y_i-y_s)/R_P$. **b** Histograms of the relative angle $\theta_{i1} = \tan^{-1}[(y_1-y_i)/(x_1-x_i)]$. **c** The distance $\Delta r_{i1}/R_P = \left[(x_1-x_i)^2 + (y_1-y_i)^2\right]^{1/2} \Big/ R_P$

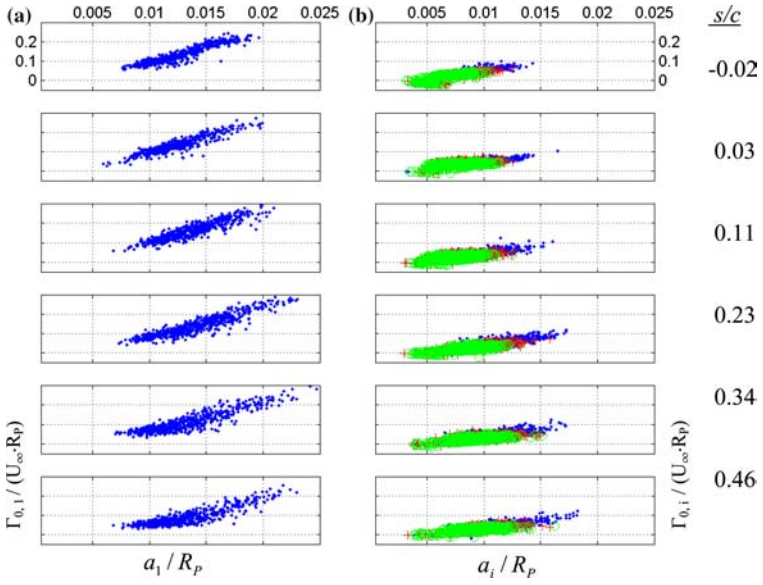

Fig. 11 **a** Primary vortex strength $\Gamma_{O,1}/U_\infty R_P$ versus radius a_1/R_P. **b** The strongest three secondary vortices $i=2$ (*diamonds*), $i=3$ (*pluses*), and $i=4$ (*open circles*) circulations $\Gamma_{O,i}/U_\infty R_P$ versus a_i/R_P

7 Velocity fluctuations produced by vortex wandering, variation in vortex strength, and the presence of multiple vortices

The mean and fluctuating velocity field properties of the tip vortex flow are influenced by: (1) the primary vortex wandering; (2) the cyclic variability in the vortex core size and strength; and (3) the presence of multiple vortices. In this section, these three effects will be studied analytically and by using simplified numerical computations of the vortex flow field. The results of this analysis of the major features of the mean and fluctuating velocity distributions will then be compared with the experimentally obtained PIV measurements of the vortical flow.

The isotropic wandering of a Gaussian line vortex will produce a time-averaged flow field that is also a Gaussian vortex, but one that has an increased core size and a reduced maximum tangential velocity (Eqs. 7 and 8). The wandering of a laminar vortex will also result in the creation of pseudo-turbulent velocity fluctuations that will peak at the center of the averaged vortex. If the wandering of the vortex is isotropic, the radial velocity fluctuations at the center of the average vortex will be non-zero, but the correlation of the in-plane velocities will be zero (i.e., $\overline{u'^2}$, $\overline{v'^2} > 0$ at the vortex center with $\overline{u'v'} = 0$). However, if the wandering is not isotropic, then the correlated in-plane velocity fluctuations will be non-zero. The mean velocity and vorticity fields produced by anisotropic wandering will be no longer axisymmetric. Rather, the iso-contours of vorticity magnitude become ellipsoidal.

The average velocity components produced by the wandering of a constant strength vortex are given by:

$$\bar{u}(x,y) = \int_{-\infty}^{\infty}\int_{-\infty}^{\infty} p(x_C,y_C)u(x-x_C,y-y_C)\mathrm{d}x_C\mathrm{d}y_C \quad (9)$$

$$\bar{v}(x,y) = \int_{-\infty}^{\infty}\int_{-\infty}^{\infty} p(x_C,y_C)v(x-x_C,y-y_C)\mathrm{d}x_C\mathrm{d}y_C \quad (10)$$

where $u(x,y)=u_\theta(r)\cos\theta$ and $v(x,y)=u_\theta(r)\sin\theta$, with $r^2=(x-x_C)^2+(y-y_C)^2$. The location of the vortex center can be described with a bivariate normal distribution

$$p(x_C,y_C) = \frac{1}{2\pi\kappa_x\kappa_y(1-\alpha^2)^{1/2}}\mathrm{e}^{-\frac{1}{2}\left(x_C^2/\kappa_x^2+y_C^2/\kappa_y^2-2\alpha x_C y_C/\kappa_x\kappa_y\right)/(1-\alpha^2)} \quad (11)$$

where κ_x and κ_y are the standard deviations, and $\alpha=(\langle x_C y_C\rangle-\langle x_C\rangle\langle x_C\rangle/\kappa_x-\kappa_y$ is the statistical correlation coefficient. The velocity fluctuations will be given by:

$$\overline{u'^2}(x,y) = \int_{-\infty}^{\infty}\int_{-\infty}^{\infty} p(x_C,y_C)(u(x-x_C,y-y_C))^2\mathrm{d}x_C\mathrm{d}y_C - \left[\int_{-\infty}^{\infty}\int_{-\infty}^{\infty} p(x_C,y_C)u(x-x_C,y-y_C)\mathrm{d}x_C\mathrm{d}y_C\right]^2 \quad (12)$$

$$\overline{v'^2}(x,y) = \int_{-\infty}^{\infty}\int_{-\infty}^{\infty} p(x_C,y_C)(v(x-x_C,y-y_C))^2\mathrm{d}x_C\mathrm{d}y_C - \left[\int_{-\infty}^{\infty}\int_{-\infty}^{\infty} p(x_C,y_C)v(x-x_C,y-y_C)\mathrm{d}x_C\mathrm{d}y_C\right]^2 \quad (13)$$

$$\overline{u'v'}(x,y) = \int_{-\infty}^{\infty}\int_{-\infty}^{\infty} p(x_C,y_C)u(x-x_C,y-y_C)v(x-x_C,y-y_C)\mathrm{d}x_C\mathrm{d}y_C - \left(\int_{-\infty}^{\infty}\int_{-\infty}^{\infty} p(x_C,y_C)u(x-x_C,y-y_C)\mathrm{d}x_C\mathrm{d}y_C\right)\cdot\left(\int_{-\infty}^{\infty}\int_{-\infty}^{\infty} p(x_C,y_C)v(x-x_C,y-y_C)\mathrm{d}x_C\mathrm{d}y_C\right) \quad (14)$$

The mean and fluctuating vorticity fields can also be computed.

If $\kappa_x = \kappa_y = \kappa$, and $\alpha = 0$, the wandering is isotropic. Calculation of the mean vorticity field will yield a Gaussian vortex with tangential velocity and vorticity distributions given by Eqs. 1 and 2, and averaged properties given by Eqs. 7 and 8. The fluctuations in vorticity can be found in closed form:

$$\frac{\overline{\omega'^2}}{\omega_c^2} = \frac{-(\eta_1/\eta_2)^2}{a_{2\kappa}(a_\kappa)^2}\left[\begin{array}{l} -4\left(\frac{\kappa}{a}\right)^4 \eta_1^2 e^{-\left(2\eta_1/a^2\right)\left(x^2+y^2/a_{2\kappa}\right)} \\ -4\eta_1\left(\frac{\kappa}{a}\right)^2 e^{-\left(2\eta_1/a^2\right)\left(x^2+y^2/a_{2\kappa}\right)} - e^{-\left(2\eta_1/a^2\right)\left(x^2+y^2/a_{2\kappa}\right)} \\ +4\eta_1\left(\frac{\kappa}{a}\right)^2 e^{-\left(2\eta_1/a^2\right)\left(x^2+y^2/a_{2\kappa}\right)} + e^{-\left(2\eta_1/a^2\right)\left(x^2+y^2/a_{2\kappa}\right)} \end{array}\right] \quad (15)$$

where $a_\kappa = 2\eta_1(\kappa/a)^2 + 1$, $a_{2\kappa} = 4\eta_1(\kappa/a)^2 + 1$, and $\omega_C = \eta_2\Gamma_O/\pi a^2 = (2U_C/a)$. The velocity fluctuations $\left(\overline{u'}^2 + \overline{v'}^2\right)\Big/U_C^2$ at the mean vortex center are given by:

$$\left.\frac{\overline{u'^2} + \overline{v'^2}}{U_C^2}\right|_{(0,0)} = \frac{1}{\eta_2^2}\cdot\frac{1}{2(\kappa/a)^2}\cdot\ln\left(\frac{a_\kappa^2}{a_{2\kappa}}\right) \quad (16)$$

where $U_C = \eta_2\Gamma_O/2\pi a$. It is possible to correct for wandering through shifting of the individual flow realizations acquired with PIV, and this will be discussed in the next section.

Figure 12 shows the mean flow profiles, the velocity fluctuations, and the vorticity fluctuations for the case of isotropic wandering of a constant strength vortex. The effect of wandering is most pronounced when the wandering amplitude is 78% of the actual core radius. Plotted in Fig. 13 are the values of the velocity fluctuations, $\left(\overline{u'}^2 + \overline{v'}^2\right)\Big/U_C^2$, and vorticity fluctuations, $\overline{\omega'}^2\Big/\omega_C^2$, for isotropic wandering as a function of wandering amplitude, at the mean wandering location ($x = 0$, $y = 0$). The peak normalized velocity fluctuations are 71% and the vorticity fluctuations are 28% at the vortex center. Also shown in Fig. 13 are the fluctuation values for a case of anisotropic wandering. In this particular case of anisotropic wandering, the peak value of the velocity fluctuations $\left(\overline{u'}^2 + \overline{v'}^2\right)\Big/U_C^2$ is 68% at a wandering amplitude of $\kappa_x/a = 1.08$. Similarly, the peak in $-\overline{u'v'}/U_C^2$is 9.5% and occurs at $\kappa_x/a = 0.77$. The peak value of $\overline{\omega'}^2\Big/\omega_C^2$ at the mean vortex center is 31% and occurs for a wandering amplitude of $\kappa_x/a = 1.05$. The correlated velocity fluctuations are small compared to the sum of the fluctuation magnitudes.

Analysis of the data in Fig. 9d reveals that the primary vortex is undergoing anisotropic wandering. The range of wandering amplitudes at the various s/c locations is measured to be $0.3 < \kappa_x/a < 1.1$ and $1.6 < \kappa_x/\kappa_y < 2.1$, with an average value of $\kappa_x/\kappa_y = 1.89$. The typical statistical correlation coefficient is $\alpha \sim 0.4$. Also plotted in Fig. 13 are the values of the velocity fluctuations, $\left(\overline{u'}^2 + \overline{v'}^2\right)\Big/U_C^2$,$\overline{u'v'}/U_C^2$, and $\overline{\omega'}^2\Big/\omega_C^2$ for anisotropic wandering with $\kappa_x/\kappa_y = 2$ and $\alpha = 1/2$ as a function of the wandering amplitude, at the mean wandering location (0,0). For the range of the experimental wandering amplitudes, the expected peak magnitude of the velocity fluctuations $\left(\overline{u'}^2 + \overline{v'}^2\right)\Big/U_C^2$ ranges from 0.25 to 0.70, the peak value of $-\overline{u'v'}/U_C^2$ ranges from 0.05 to 0.10, and the value of the vorticity fluctuations at the mean vortex center ranges from 0.05 to 0.3. We will compare these predicted values to the measured fluctuations in the next section.

Next, we consider the case of a line vortex that is not wandering, but is randomly changing its strength and core size. The averaged vortex strength measured in a plane perpendicular to the axis would be given by:

$$\overline{\Gamma(r)}_C = \int_0^\infty\int_0^\infty p(\Gamma_O, a)\Gamma_O\left(1 - e^{-\eta_1(r/a)^2}\right)d\Gamma_O da \quad (17)$$

where $p(\Gamma_{O,\ a})$ is a probability density function for the vortex parameters. If the core size and circulation are correlated with $\Gamma_O = \beta a$, then the average vortex strength is given by:

$$\overline{\Gamma(r)}_C = \int_0^\infty p_v(a)\beta a\left(1 - e^{-\eta_1(r/a)^2}\right)da \quad (18)$$

Figure 8c shows the distribution of the vortex radii, and suggests that the distribution of the core radii roughly approximates a normal distribution. For illustration purposes, we use the normal distribution given by:

$$p_v(a) = \frac{1}{\kappa_v\sqrt{2\pi}}e^{-\frac{1}{2}\left(\frac{a-\langle a\rangle}{\kappa_v}\right)^2} \quad (19)$$

with mean $\langle a\rangle$ and standard deviation κ_v. The results for varying values of $\kappa_v/\langle a\rangle$ are shown in Fig. 14. (Note that we have excluded negative values of the core radius and vortices with radii larger than $\langle a\rangle + 5\kappa_v$). Here, $\beta = 37.1$ m/s, which is the average slope derived from the data in Fig. 11a. For small levels of core-size fluctuations, the resulting average vortex approaches that of a Gaussian vortex (Fig. 14a). Increasing levels of fluctuation result in a reduction of the peak velocity of the

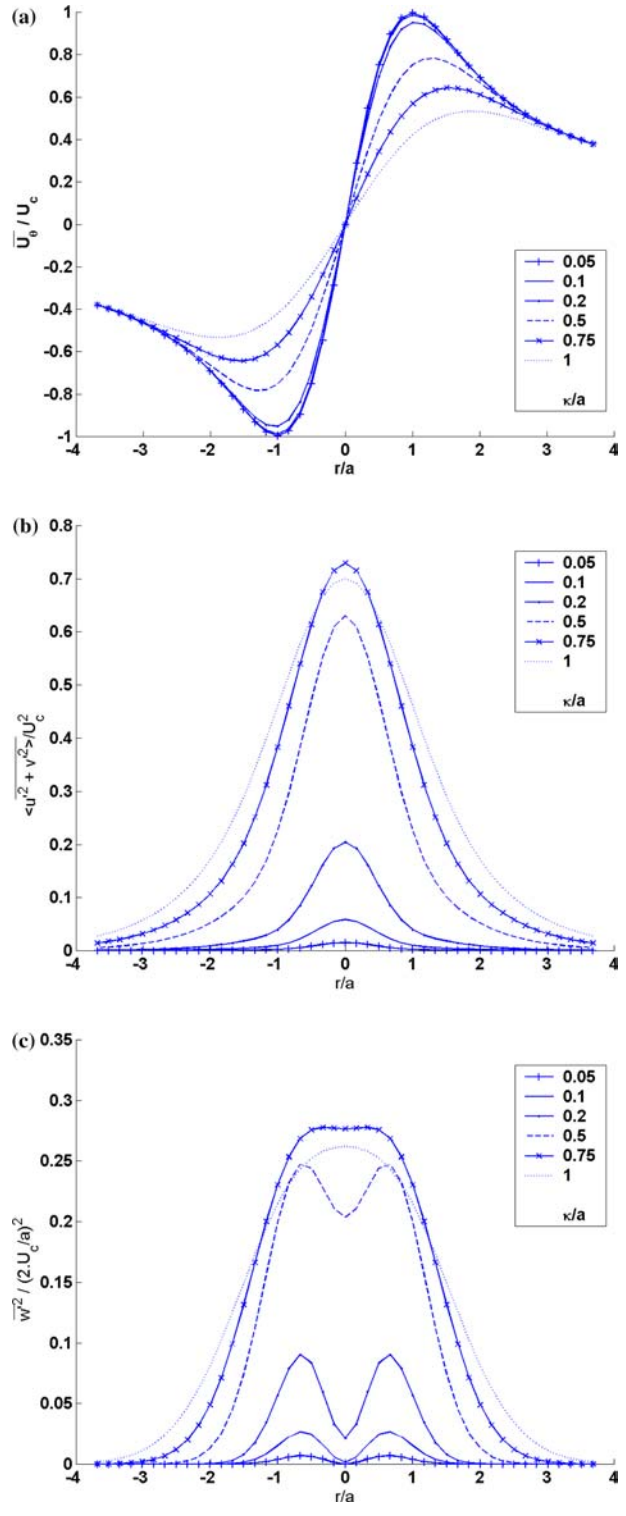

Fig. 12a–c Average flow profiles produced by the isotropic wandering of a Gaussian vortex with varying amplitudes κ/a. **a** Average circumferential velocity as a function of radial distance, $\overline{u_\theta}/U_C$. **b** Velocity fluctuations $(\overline{u'^2}+\overline{v'^2})\Big/U_C^2$. **c** Vorticity fluctuations $\overline{\omega'^2}\Big/\omega_C^2$

averaged vortex and a flattening of the velocity distribution. The apparent velocity fluctuations, $\left(\overline{u'^2}+\overline{v'^2}\right)\Big/U_C^2$, are shown in Fig. 14b. Small-amplitude fluctuations in the core size result in two annuli of increased velocity variability, the first occurring within one core radius of the averaged vortex, and the second at approximately twice the core radius of the averaged vortex. The velocity fluctuations on the mean vortex axis remain at zero. The peak magnitudes of $\left(\overline{u'^2}+\overline{v'^2}\right)\Big/U_C^2$ continue to grow as the magnitude of the vortex variability grows. However, the relative magnitude of the velocity fluctuations is small for the flow considered here. Figure 14c shows that the vorticity fluctuations become unbounded near the vortex center. For $\kappa_v/\langle a\rangle = 0.2$, two annuli around the center can be noticed, one annulus of reduced fluctuations at $r/\langle a\rangle \cong 0.5$, and one of increased fluctuations at $r/\langle a\rangle \cong 1$, with a magnitude less than 0.05. Examination of Fig. 8c indicates that $\kappa_v/\langle a\rangle \sim 0.2$, making the expected peak values of $\left(\overline{u'^2}+\overline{v'^2}\right)\Big/U_C^2 < 0.02$. This is much less than the fluctuations due to wandering.

Lastly, pseudo-turbulence is produced by the presence of multiple vortices when the relative location of the vortices is variable. The location of the secondary vortex with respect to the primary vortex is not random, as seen in Fig. 10. However, a simple model of the flow can be constructed with two vortices: a stationary primary vortex and a weaker, secondary vortex positioned at a given radius and angular orientation. We will consider the case where the angular position of the secondary vortex is random (i.e., having uniform probability distribution) and the radial position varies with a normal distribution about a mean value. Velocity fluctuations would be created due to the motion of the secondary vortex. The magnitude of the induced fluctuations near the core of the primary vortex would scale with $\sim\Gamma_2/(\Gamma_1\delta)$, where δ is the magnitude of the separation between the axes of the two vortices. In the flow examined here, $0.2 < \Gamma_2/\Gamma_1 < 1.0$ and $\langle\delta\rangle/\langle a_1\rangle \sim 2$. Figure 15 shows the average flow profiles when the secondary vortex is positioned randomly in the azimuthal direction around the primary vortex with a mean radial position of $\langle\delta\rangle/\langle a_1\rangle = 1.6$. L is the distance separating the perimeters of the two cores ($L = \delta - a_1 - a_2$) and has a normal distribution with a mean value of $a_1/10$ and varying fluctuation amplitudes κ. Only the positive part of the distribution is used (i.e., the cores are not allowed to overlap). The core size and circulation of the stationary (primary) vortex are twice those of the secondary orbiting vortex. The mean profiles of the primary vortex are modified by the presence of the secondary vortex, with a broadening of the region of maximum velocity. A ring of velocity and a ring of vorticity fluctuations are produced by the presence of the second vortex, and the positions of the peak fluctuations are outside the core of the primary vortex for this degree of separation. The largest fluctuations occur for the smallest amplitudes of variation. The velocity fluctuations in the core of the primary vortex can be significant, with magnitudes of approximately 0.20.

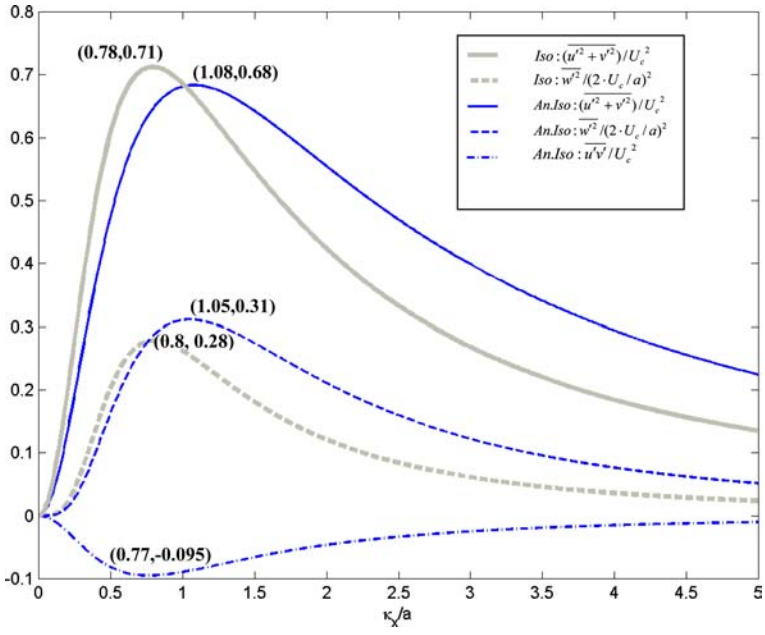

Fig. 13 The magnitudes of fluctuations at the origin for the cases of isotropic and anisotropic wandering of a Gaussian vortex as a function of wandering amplitude; $(\overline{u'}^2+\overline{v'}^2)/U_C^2$ and $\overline{\omega'}^2\Big/\omega_C^2$ as a function of κ/a for isotropic wandering; the same and $\overline{u'v'}/U_C^2$ for varying κ_x/a, given $\kappa_x=2\kappa_y$ and $\alpha=1/2$. Noted on the figure are the coordinates of the peak values

8 Measured velocity fluctuations

The average and fluctuating velocity and vorticity fields were calculated from the experimental data. The PIV measurements were resolved on the order of ten velocity vectors across the diameter of the primary vortex, and these measurements were spatially averaged due to the overlap of the PIV interrogation windows. Consequently, we do not expect to resolve the smallest scales of velocity fluctuations in the vortical flow. However, with the instantaneous flow fields, it is possible to determine how vortex variability and wandering contribute to the apparent velocity fluctuations derived from the analysis of the averaged flow field.

In order to understand the effect of vortex wandering, variable vortex strength, and the presence of multiple vortices on the measured flow variability, the individual flow fields can be scaled to reduce these effects. First, the effect of the primary vortex wandering can be reduced by the in-plane shifting of the individual flow fields such that the axes of the primary vortices are aligned before averaging and calculating the velocity fluctuations. However, the spatial shifting of the individual images does not account for the variability of the strength and core size of the individual primary vortices. This effect can be reduced by internally scaling each instantaneous flow field with the identified primary vortex circulation and core size, a_1 and $\Gamma_{O,1}$, derived from each individual realization, resulting in normalized core radius and strength of unity.

Figure 16 shows the average vorticity field from three types of analyses: the simply averaged (unmodified) vorticity fields; the shifted vorticity fields; and the internally scaled and shifted vorticity fields. The unmodified mean field vorticity contours indicate that the peak vorticity of the primary vortex increases with downstream distance until it peaks at $s/c=0.11$, and, thereafter, it drops to a minima at $s/c=0.46$. A different trend is seen when the instantaneous PIV fields are shifted to co-locate the primary vortex centers before averaging. After a moderate increase in the peak vorticity of the primary vortex from $s/c=-0.02$ to $s/c=0.03$, its magnitude remains essentially invariant for the investigated range. The shifted and scaled vorticity fields show an increase in the peak vorticity with s/c, until it reaches a maximum for $0.11<s/c<0.23$, whereafter, it decreases. The iso-contours of the shifted and scaled vortices are approximately circular for $s/c=-0.02$, 0.03, and 0.11. The remaining contours are elliptical. In these cases, the presence of the secondary vortices continues to distort the average vorticity fields.

Shifting and scaling will reduce the apparent velocity fluctuations. Figure 17a shows the uncorrelated velocity fluctuations $\left(\overline{u'}^2+\overline{v'}^2\right)\Big/U_C^2$ computed directly (no shifting or scaling). The velocity fluctuations are normalized using $U_C=\eta_2\overline{\Gamma_{O,1}}/(2\pi\overline{a_1})$, the maximum tangential velocity of the primary vortex based on the circulation and core size derived from the averaged flow field. Large velocity fluctuations are seen in the cores of the vortices, with magnitudes of around 0.2. Next, the images are shifted and the averages computed. The results are shown in Fig. 17b. Here, the turbulent quantities are normalized by $\eta_2\overline{\Gamma_{O,1,\mathrm{Shifted}}}\Big/\left(2\pi\overline{a_{1,\mathrm{Shifted}}}\right)$, derived from the average flow field *after* the shifting has been performed. The velocity fluctuations associated with the primary vortex are reduced to ~0.1 or 50% of the un-shifted value for $s/c\le 0.23$. This suggests that the wandering amplitude is relatively small for these cases where $\kappa/\langle a\rangle<0.5$, and this reduction is consistent

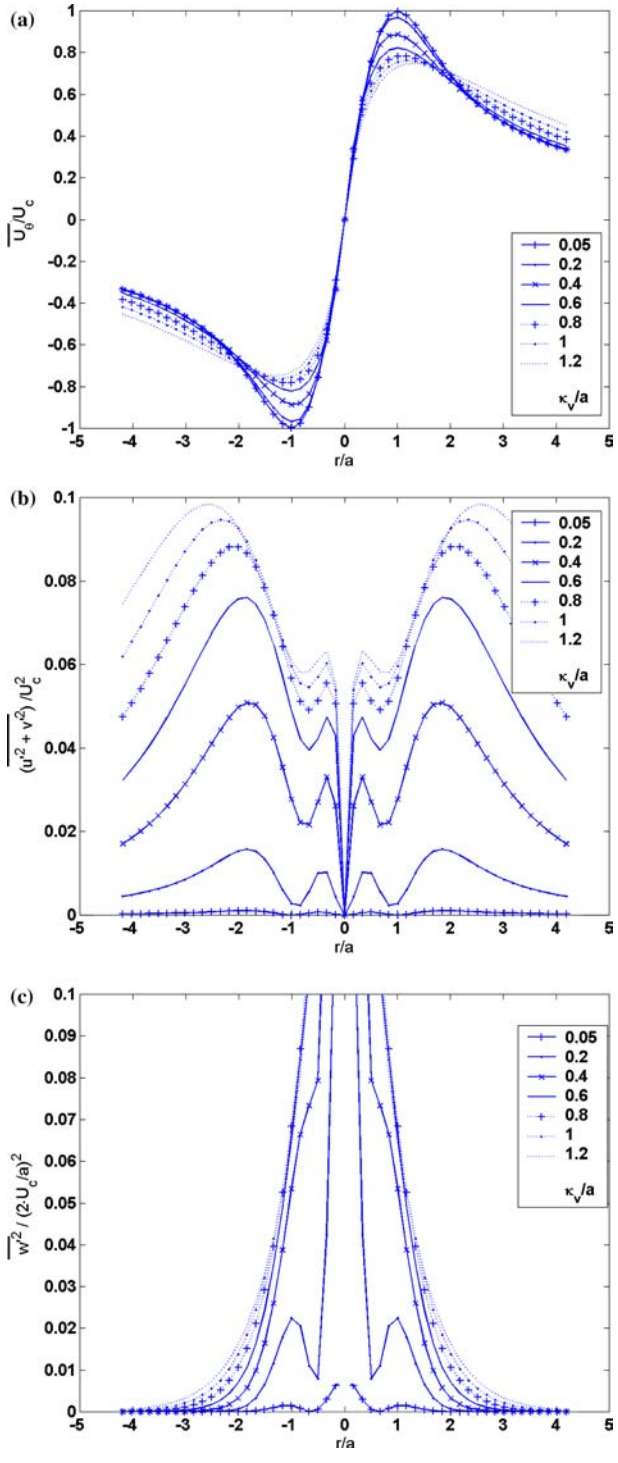

Fig. 14a–c The flow profiles created by a Gaussian vortex with varying core size, and the strength being a linear function of the core size. **a** Average circumferential velocity as a function of radial distance, $\overline{u_\theta}/U_C$. **b** Velocity fluctuations $\left(\overline{u'}^2+\overline{v'}^2\right)\Big/U_C^2$. **c** Vorticity fluctuations $\overline{\omega'}^2\Big/\omega_C^2$

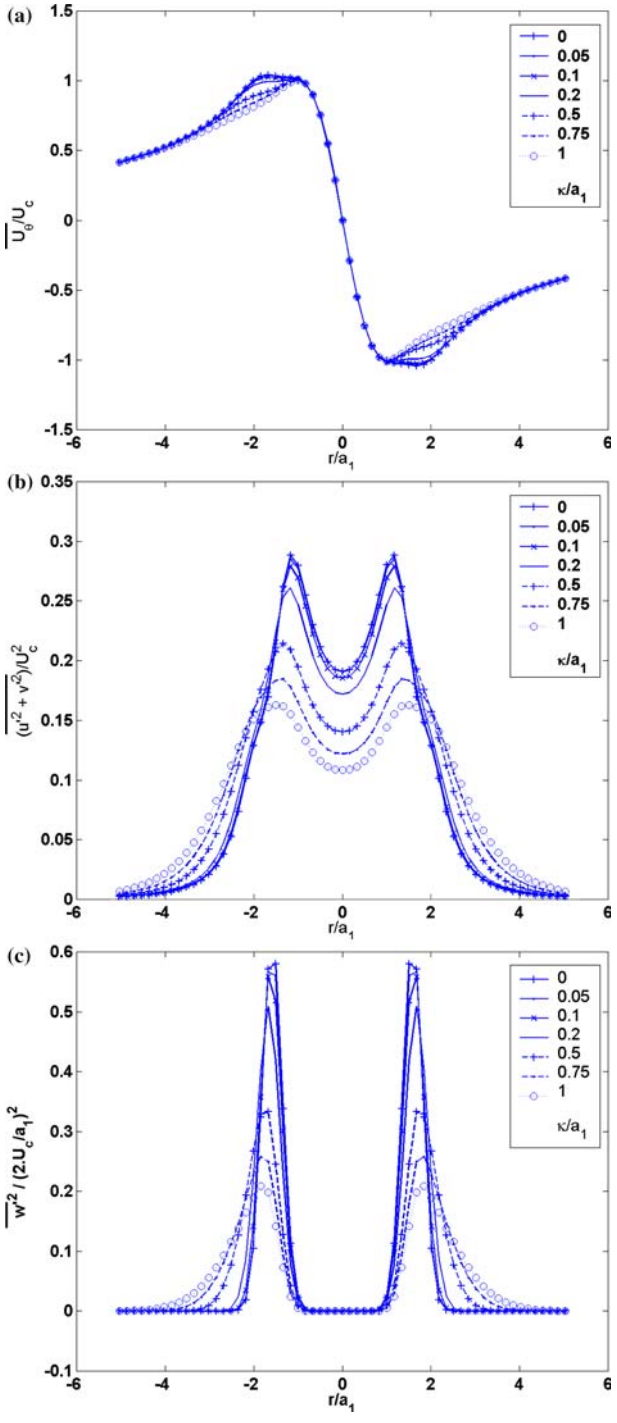

Fig. 15a–c Average flow profiles produced by a secondary vortex with varying radial position and random circumferential position relative to the position of a primary vortex. The radial distance between the vortices is a_1+a_2+L, and L has a normal distribution with varying amplitudes κ/a_1 with $\overline{L}=a_1/10$. **a** Average circumferential velocity as a function of radial distance, $\overline{u_\theta}/U_C$. **b** Velocity fluctuations $\left(\overline{u'}^2+\overline{v'}^2\right)\Big/U_C^2$. **c** Vorticity fluctuations $\overline{\omega'}^2\Big/\omega_C^2$

with the predicted fluctuating magnitudes from pure wandering, as discussed in the previous section. However, the magnitude of the fluctuations has remained the same for $s/c=0.34$ and has *increased* for $s/c=0.46$. In these cases, the wandering amplitudes are the largest, but shifting is not sufficient to reduce the apparent fluctuations. The fluctuations in the wake-spiral have also increased, indicating that the secondary vortices are

not strongly spatially correlated with the primary vortex. The resulting velocity fields are then shifted and internally scaled, and the velocity fluctuations are computed and then normalized with $\eta_2\overline{\Gamma_{O,1}}/(2\pi\overline{a_1}) = 0.114$. Figure 17c plots the resulting fluctuations $((ua_1/\eta_2\Gamma_{O,1})')^2 + ((va_1/\eta_2\Gamma_{O,1})')^2$ in spatial coordinates $[(x/a_1), (y/a_1)]$. The residual fluctuations near the primary vortex axis increase, with the largest increases occurring downstream. Indeed, the velocity fluctuations value at $s/c = 0.34$ is $\sim$0.6, and at $s/c = 0.46$, it is $\sim$1.1. The process of shifting and scaling has revealed how the presence of the uncorrelated secondary vortices can lead to relatively large velocity fluctuations.

The same procedure was used to compute the correlated velocity fluctuations, $-\overline{u'v'}/U_C^2$. Figure 18 presents the resulting fields. The process of shifting significantly reduces the magnitude of the correlated velocity fluctuations on the vortex axis (Fig. 18b), indicating that the correlated velocity fluctuations largely result from the wandering of the primary vortex. Yet, scaling and shifting of the instantaneous fields before the calculations, Fig. 18c, increase the correlated velocity fluctuations at the center of the primary vortex, suggesting that the velocities induced by the secondary vortices have lead to the creation of these fluctuations.

Figure 19 presents the results for the vorticity fluctuations, $\overline{\omega'^2}/\omega_C^2$. Here, shifting and scaling significantly reduces the magnitude of the fluctuations at the center of the primary vortex (Fig. 19c). However, an annulus of strong vorticity fluctuations is found at $s/c = 0.34$ and 0.46. The magnitude and location of the peak vorticity fluctuations are consistent with the analysis of the multiple-vortex effect, where the presence of secondary vortices leads to the creation of a ring of vorticity fluctuations outside the core of the primary vortex.

We have considered the individual effects of the three contributors to variability, and have discovered that the magnitudes of the measured variability are of similar magnitude to those expected from the canonical modeling in Sect. 7. A fourth cause for velocity fluctuations would be the presence of unresolved smaller-scale vorticity in the flow fields (turbulence), and some of the remaining variability may, in fact, be the result of turbulence. The corrections used here can result in the reduction or increase in the relative level of measured variability. But it is not necessarily appropriate to consider the remaining variability solely due to turbulent flow, since there are other sources of error that have not been corrected, especially the presence of multiple uncorrelated vortices.

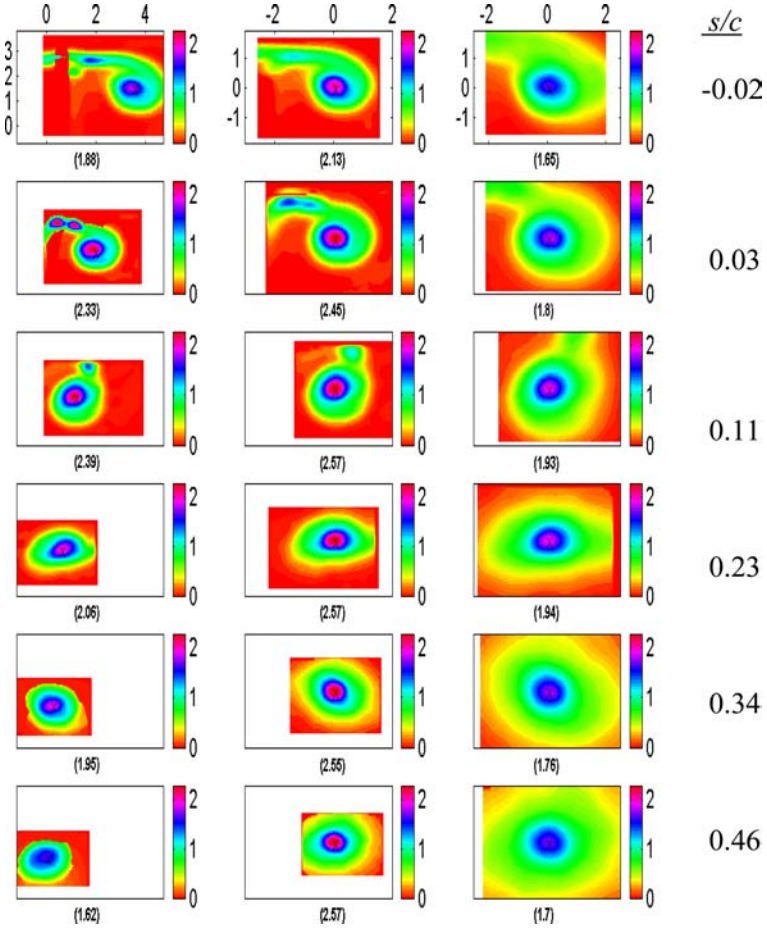

Fig. 16a–c The vorticity magnitude as a function of downstream distance s/c. **a** The average field, $\overline{\omega}/(2\overline{U_C}/\overline{a_1})$ plotted in $[x/\bar{a}, y/\bar{a}]$. **b** The average flow field after the centers of the primary vortices have been shifted, $\overline{\omega}/(2\overline{U_C}/\overline{a_1})_{\text{Shifted}}$. **c** The average flow field after the instantaneous images were scaled and shifted, $\overline{\omega/(2U_C/a_1)}$, plotted in $[x/a_1, y/a_1]$. The *crosses* show the location of the center of the identified vortex, and the value in parentheses is the magnitude at that location

9 Vortex roll-up, unsteadiness, and cavitation inception

The analysis of the *average* flow fields shows that the primary vortex merges with weaker secondary and wake vortices. Figures 5 and 6 indicate that the position of the primary-to-secondary merger occurs at $s/c \sim 0.23$. If the merging of the two strongest vortices does occur in reality in the tip vortex flow, then they are expected to produce a single vortex after undergoing a highly turbulent mixing process. Devenport et al. (1999) examined how two co-rotating laminar vortices of equal strength merged to form a single vortex having nearly the sum of the circulations of the original vortices. However, during the merging process, finer filaments of vorticity were produced between the orbiting pair of vortices that were similar to the streamwise "braids" observed between the primary large-scale vortices of shear layers and jets. Once the vortices merged, the core of the single vortex was turbulent, but the flow in the core relaxed to become laminar with a surrounding region of turbulence. The final core area of the merged vortex was approximately 3.5 times that of the combined area of the original vortices.

Several features of the process observed in this study bear a resemblance to those observed in the merger of co-rotating vortices. Nonetheless, significant differences could be noticed also. First, as shown in Fig. 6, the average strength of the instantaneous primary vortex, $\langle \Gamma_{O,1} \rangle$, is steady or decreasing with downstream distance, and the core size $\langle a_1 \rangle$ remains relatively constant. It is possible that the secondary vortex is spiraling around the primary vortex, tilting its axis, and, thus, reducing the magnitude of the vorticity in the imaging plane. The fact that the core of the primary vortex is not increasing with downstream distance indicates that the vortices have *not* completed their merger. However, the amount of variability increases significantly after the position where the secondary vortex is no longer discernable in the mean flow field.

It is likely that, instead of a nearly symmetric merger of two vortices, complex vortex–vortex interaction is taking place between the primary and secondary vortices. Such three-dimensional vortex interactions have been observed by Savas and co-workers (Chen et al. 1999 and Ortega et al. 2003). They have studied how two unequal strength co-rotating vortices merge into a single structure after a three-dimensional unsteady process, characterized by the fragmentation of the weaker vortex into filaments under the effect of the stronger vortex. Some of the fragmented filaments merge with the strong vortex. However, other filaments do not merge and orbit around the interaction instead. They have also shown how counter-rotating vortices of unequal strength can undergo an instability that results in the wrapping of the

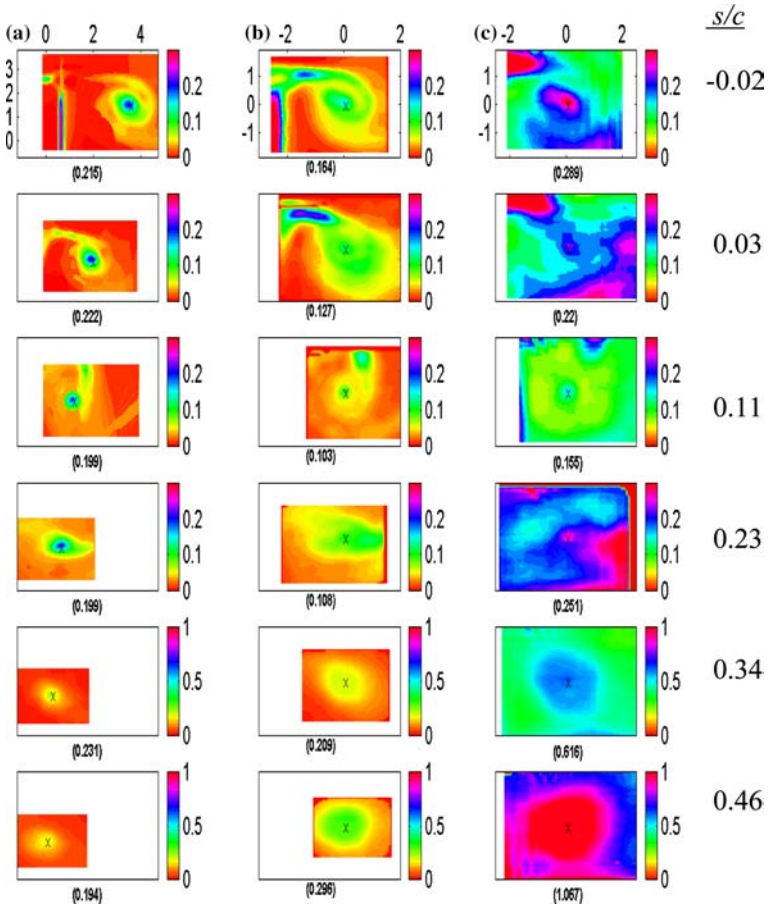

Fig. 17 The velocity fluctuations $\left(\overline{u'}^2 + \overline{v'}^2\right) \Big/ \overline{U_C}^2$; otherwise, the same as in Fig. 16

weaker vortex around the stronger one. The onset of this wrapping can occur relatively far downstream of the position of the vortices' formation. When the secondary vortex is captured by the field of the primary vortex, the unsteadiness of the flow significantly increases. The significant increase in unsteadiness downstream near $s/c \approx 0.46$ may, therefore, result from such complex vortex–vortex interactions. The resolution of such a complex flow is not possible with the planar PIV system used here.

While it was not possible to directly measure the smaller scales of vorticity, observations of cavitation inception in the wake of the rotor provided circumstantial evidence that these vortical interactions are occurring. These interactions lead to the formation, convection, and stretching of both large- and fine-scale concentrated vorticity, and this could cause a significant reduction of pressure within the cores of the vortices and the formation of cavitation bubbles. Chesnakas and Jessup (2003) detail these cavitation observations. As the static pressure of the test section was lowered during the operation, transient cavitation was detected in the wake of the rotor. The regions of lowest *average* pressure are in the cores of the strongest vortices and the minimum average pressure, $\overline{C_P}$, and the minimum instantaneous pressure coefficient, $\langle C_P \rangle$, occurs at $s/c \approx 0.1$, as shown in Fig. 7. Consequently, it was expected that the location of cavitation inception (the first discernable detection of cavitation) would occur between $0.1 < s/c < 0.2$. However, the first incipient cavitation bubbles were observed further downstream around $s/c \approx 0.46$, which coincides with the region of increased flow variability observed in Fig. 19.

Cavitation inception occurs when microbubbles (nuclei) in the free stream experience a reduction in static pressure below a critical level that is related to their original size (Oweis et al. 2005c). If the pressure remains low, the bubbles will continue to grow, but if the pressure reduction is transient, the bubbles will collapse, often producing a sharp acoustic pulse (see Brennen (1995) and Oweis et al. (2004) for a more complete discussion). In the present flow, cavitation was detected acoustically, as very small cavitation bubbles formed and collapsed in the tip region of the rotor. Chesnakas and Jessup (2003) describe the setup whereby images were taken of the small cavitation bubbles using an acoustic trigger and a post-trigger delay on a digital video camera. Cavitation inception did not occur in the region of lowest mean pressure. Instead, the first detectable cavitation bubbles transpired for $0.4 < s/c < 0.5$, which is the region of increased flow unsteadiness revealed by the instantaneous flow fields.

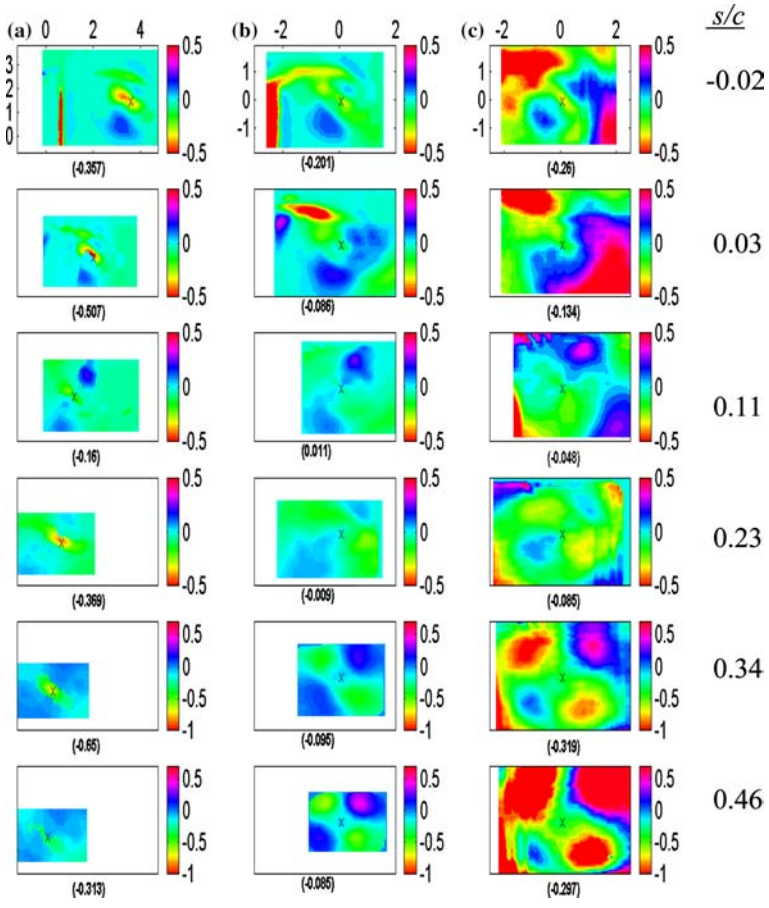

Fig. 18 The velocity fluctuations $-10 \times \overline{u'v'} \Big/ \overline{U_C}^2$; otherwise, the same as in Fig. 16

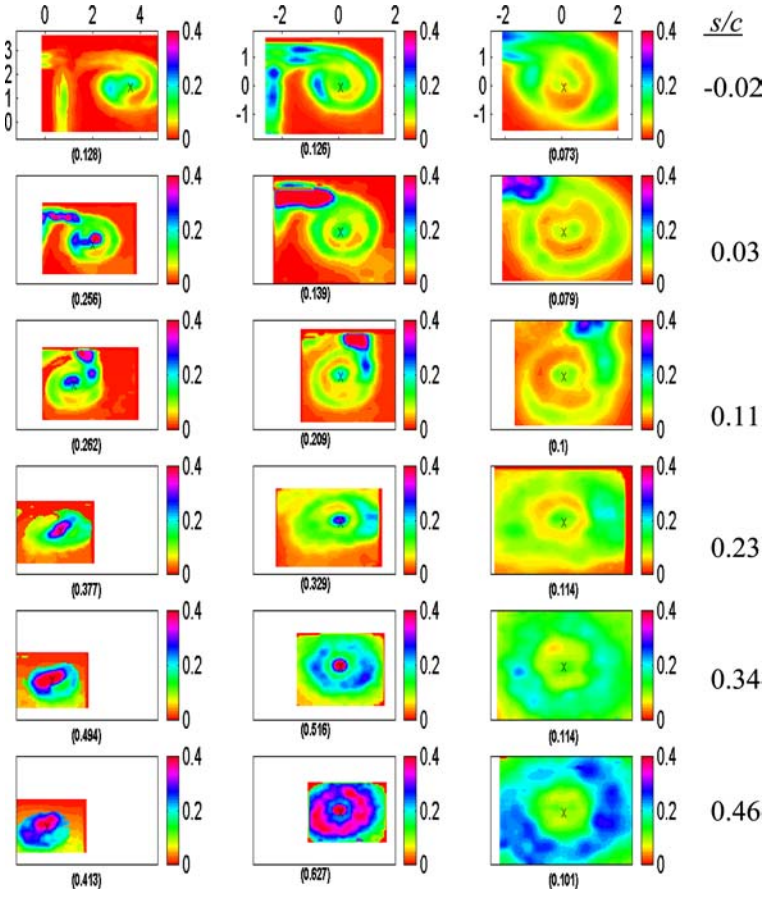

Fig. 19 The vorticity fluctuations $\overline{\omega'^2}\Big/\left(2\overline{U_C}/\overline{a_1}\right)^2$; otherwise, the same as in Fig. 16

Furthermore, the free stream pressure at cavitation inception was much higher than the inception value that was expected based on the values of the average pressure coefficient, $\overline{C_P}$, and the minimum instantaneous pressure coefficient, $\langle C_P \rangle$, at $s/c \sim 0.1$. Inception is expected when the minimum pressure reaches or drops below the vapor pressure. In this case, this occurs when $C_P \leqslant -\sigma_\infty = (P_\infty - P_v)/\frac{1}{2}\rho U_\infty^2$. Here, Eq. 5 is used to estimate the pressure in the vortex core and P_V is the liquid vapor pressure. During the process of vortex roll-up, the minimum average pressure coefficient $\overline{C_P}$ was approximately -6.0 at $s/c \approx 0.1$. Similarly, $\langle C_P \rangle$ varied between -4 and -8. Cavitation might occur in this region first, even if $C_P > -\sigma_\infty$, since there could be intermittent vortices with sufficient strength to produce significant pressure depressions. Such vortices are relatively rare, but a small number were identified from the pressure coefficient histogram at $s/c = 0.11$ (Fig. 8d).

However, cavitation inception was not found to occur at $s/c \approx 0.1$. Instead, the first appearance of cavitation was at $s/c \approx 0.5$. Inception was noted when a discrete cavitation event occurred approximately once every ten seconds. Averaged over the three blades, the inception cavitation number was 11 for the flow presented here. Transient cavitation bubbles occurred where $\overline{C_P}$ was between -2.5 and -3.5 and where $\langle C_P \rangle$ varied between -1 and -4, making the average pressure coefficient substantially higher than the pressure needed for inception. The pressure coefficient histograms at this location showed a reduced probability that individual vortices would experience sufficiently low pressures for inception.

Magnified images of the bubbles showed that they were often quite small (less than 1 mm in size), and it was difficult to resolve their shape. Yet, some bubbles at their maximum volume were observed to be elongated and/or of a spiral shape. This suggests that the bubbles were forming in the cores of very small vortices undergoing complex flow processes that resulted in a transient reduction of pressure. Katz and O'Hern (1986), O'Hern (1990), and Iyer and Ceccio (2002) examined cavitation inception and development in plane shear layers. Inception occurs first within the streamwise vortices of the shear layer. The streamwise vortices are stretched between the spanwise vortices, resulting in a reduction in the vortex diameter and a transient reduction in the core pressure of these streamwise vortices or "braids." Further reduction in the overall flow pressure will then lead to cavitation in the spanwise vortices. This phenomenon has been observed in axisymmetric jets (see Ran and Katz (1994), Gopalan et al. (1999), and Arndt (2002)). These studies have demonstrated that the actual incipient cavitation number is often much higher than the predicted value based on the mean pressure deficit occurring in the cores of the vortices with the highest strength (i.e., the spanwise vortices in plane shear layers

and the cross-stream vortices of a jet). Inception occurs in the smaller, weaker vortices that are stretched by the stronger ones. As the pressure is further reduced, the cores of these larger vortices will eventually cavitate and fill with vapor, and this has also been observed in the present study. A reduction of the cavitation number to $\sim$0.55 resulted in vaporization within the cores of the primary and secondary vortices, as shown in Fig. 2. This is the expected inception value based on $\langle C_P \rangle \sim \sigma_\infty$ at the position of mean minimum pressure, $s/c \approx 0.1$.

Devenport et al. (1999) examining the merger of equal-strength co-rotating vortices and Savas and co-workers examining the interaction of unequal pairs of co-rotating vortices (Chen et al. 1999) and counter-rotating vortices (Ortega et al. 2003) have demonstrated that small-scale vortex filaments can be created and stretched during these complex vortex interactions. In the present flow, it appears that these interactions are occurring at $s/c \approx 0.5$, leading to the transient stretching of small-scale vorticity and resulting in incipient cavitation. The flow visualization methods employed here are not able to directly resolve the small-scale vortical interactions. However, indirect evidence of these interactions are manifest in the increased relative variability of the flow field near the position of cavitation inception and the change of the structure of the flow in this region.

10 Conclusions

The interpretation of average flow fields must be performed with care when multiple regions of compact vorticity are present, as is the case of the flow downstream of a rotor tip. Parameters of the vortical flow that can be identified in the average flow field are often significantly different from instantaneously identified properties. Interpretation of flow variability must also be performed with care. The process of averaging will mask the presence of uncorrelated secondary vortices that may remain distinct in the instantaneous flow realizations. Vortex wandering and the presence of multiple vortices can lead to the production of significant velocity fluctuations. However, the velocity fluctuations resulting from spatially uncorrelated secondary vortices can be of similar magnitude to the fluctuations resulting from the wandering of the primary vortex. Image shifting and scaling can reduce the effect of primary vortex wandering and varying vortex strength (if the circulation variation is correlated with the vortex size). But, fluctuations due to the presence of multiple, uncorrelated secondary vortices will be accentuated.

Shifting and scaling of individual flow fields can reveal changes in flow variability that are otherwise masked by the process of vortex wandering. In the flow under consideration here, significant relative variability is found downstream of the blade trailing edge. Along with the observations of cavitation inception, this flow variability suggests that three-dimensional vortex interactions are taking place. These changes in relative flow variability are not apparent in the unscaled average flow fields. It is only after shifting and scaling that this flow feature is revealed.

Acknowledgements The authors acknowledge the contributions of Dr. Stuart Jessup, Dr. Christopher Chesnakas, and Dr. David Fry during the design and implementation of the experiment and would like to thank them for their permission to use the images in Figs. 1 and 2. This work was funded by the Office of Naval Research under grant number N00014-99-1-0307, with Dr. Ki-Han Kim as the technical monitor.

References

Arndt REA (2002) Cavitation in vortical flows. Annu Rev Fluid Mech 34:143–175

Baker GR, Barker SJ, Bofah KK, Saffman PG (1974) Laser anemometer measurements of trailing vortices in water. J Fluid Mech 65:325–336

Balzani N, Scarano F, Riethmuller ML, Breugelmans FAE (2000) Experimental investigation of the blade-to-blade flow in a compressor rotor by digital particle image velocimetry. ASME J Turbomachinery 122:743–750

Boulon OB, Callenaera M, Franc J-P, Michel J-M (1999) An experimental insight into the effect of confinement on tip vortex cavitation of an elliptic hydrofoil. J Fluid Mech 390:1–23

Brennen CE (1995) Cavitation and bubble dynamics. Oxford University Press, Oxford

Chen AL, Jacob JD, Savas Ö (1999) Dynamics of corotating vortex pairs in the wakes of flapped airfoils. J Fluid Mechanics 382:155–193

Chesnakas C, Jessup S (2003) Tip vortex induced cavitation on a ducted propulsor. In: Proceedings of the 4th ASME-JSME joint fluids engineering conference, Honolulu, Hawaii, July 2003, FEDSM2003–45320

Chow YC, Uzol O, Katz J, Meneveau C (2002) An investigation of axial turbomachinery flows using PIV in an optically-unobstructed facility. In: Proceedings of the 9th international symposium on transport phenomena and dynamics of rotating machinery, Honolulu, Hawaii, February 2002

Copland CM, Coton FN, Galbraith RA (1998) An experimental study on the idealised vortex system of a novel rotor blade tip. Aeronautical J 102(1017):385–392

Day KM, Lawless P, Fleeter S (1996) Particle image velocimetry measurements in a low speed research turbine. AIAA paper no. 96–2569

Devenport WJ, Rife MC, Liapis SI, Follin G (1996) The structure and development of a wing-tip vortex. J Fluid Mech 312:67–106

Devenport WJ, Zsoldos JS, Vogel CM (1997) The structure and development of a pair of counter-rotating wing-tip vortices. J Fluid Mech 332:71–104

Devenport WJ, Vogel CM, Zsoldos JS (1999) Flow structure produced by the interaction and merger of a pair of co-rotating wing-tip vortices. J Fluid Mech 394:357–377

Farrell KJ, Billet ML (1994) A correlation of leakage vortex cavitation in axial-flow pumps. J Fluids Eng 116:551–557

Figliola RS, Beasley DE (2000) Theory and design for mechanical measurements, 3rd edn. Wiley, New York, pp. 132–138

Fouras A, Soria J (1998) Accuracy of out-of-plane vorticity measurements derived from in-plane velocity field data. Exp Fluids 25:409–430

Gogineni S, Goss L, Copenhaver W, Gorrell S (1997) Development of digital two-color PIV for turbomachinery applications. AIAA paper no. 97–0494

Gopalan S, Katz J, Knio O (1999) The flow structure in the near field of jets and its effect on cavitation inception. J Fluid Mech 398:1–43

Gopalan S, Katz J, Liu HL (2002) Effect of gap size on tip leakage cavitation inception, associated noise and flow structure. J Fluid Eng 124(4):994–1004

Green SL (1995) Fluid vortices. Kluwer, Dordrecht, The Netherlands

Iyer CO, Ceccio SL (2002) The influence of developed cavitation on the flow of a turbulent shear layer. Phys Fluids 14(10):3414–3431

Judge C, Oweis GF, Ceccio SL, Jessup S, Chesnakas C, Fry DJ (2001) PIV Measurements of a tip leakage vortex. In: Proceedings of the 4th international symposium on cavitation (CAV 2001), Pasadena, California, June 2001

Katz J, O'Hern TJ (1986) Cavitation in large scale shear flow. Trans ASME J Fluids Eng 108:373–376

Lakshminarayana B (1996) Fluid dynamics and heat transfer of turbomachinery. Wiley, New York

O'Hern TJ (1990) An experimental investigation of turbulent shear flow cavitation. J Fluid Mech 215:365–391

Ortega JM, Bristol RL, Savas Ö (2003) Experimental study of the instability of unequal-strength counter-rotating vortex pairs. J Fluid Mech 474:35–84

Oweis GF, Choi J, Ceccio SL (2004) Dynamics and noise emissions of laser induced bubbles in a vortical flow field. J Acoust Soc Am, 115(3):1049–1058

Oweis GF, Jessup SD, Chesnakas CJ, Fry DJ, Ceccio SL (2005a) Development of a tip-leakage flow. Part 1: the flow over a range of Reynolds numbers. ASME J Fluids Eng (accepted)

Oweis GF, Jessup SD, Chesnakas CJ, Fry DJ, Ceccio SL (2005b) Development of a tip-leakage flow. Part 2: comparison between the ducted and unducted rotor. ASME J Fluid Eng (accepted)

Oweis GF, van der Hout IE, Iyer C, Tryggvason G, Ceccio SL (2005c) Capture and inception of bubbles near line vortices. Phys Fluids 17(2):Art.no. 022105

Raffel M, Willert C, Kompenhans J (1998) Particle image velocimetry. A practical guide. Springer, Berlin Heidelberg New York

Ran B, Katz J (1994) Pressure fluctuations and their effect on cavitation inception within water jets. J Fluid Mech 262:223–263

Spalart PR (1998) Airplane trailing vortices. Annu Rev Fluid Mech 30:107–138

Straka WA, Farrel KJ (1992) The effect of spatial wandering on the experimental laser velocimetry measurements of the end-wall vortices in an axial flow pump. Exp Fluids 13:163–170

Uzol O, Chow YC, Katz J, Meneveau C (2002) Experimental investigation of unsteady flow field within a two-stage axial turbomachine using particle image velocimetry. ASME J Turbomachinery 124:542–552

von Karman Institute for Fluid Dynamics (1997) Lecture series von Karman Institute for Fluid Dynamics, vol. 1. Rhode Saint Genèse, Belgium, ISSN 0377-8312

Wernet MP (2000) Development of digital particle image velocimetry for use in turbomachinery. Exp Fluids 28:97–115